Recurrent solutions of the Alber equation initialized by Joint North Sea Wave Project spectra

A. Ribal[1,‡], A. V. Babanin[1,†], I. Young[2], A. Toffoli[1] and M. Stiassnie[3]

[1]Centre for Ocean Engineering, Science and Technology, Swinburne University of Technology, Melbourne, VIC 3122, Australia

[2]The Australian National University, Canberra, ACT 0200, Australia

[3]Faculty of Civil and Environmental Engineering, Technion-Israel Institute of Technology, Haifa 32000, Israel

Linear instability of two-dimensional wave fields and its concurrent evolution in time is here investigated by means of the Alber equation for narrow-banded random surface waves in deep water subject to inhomogeneous disturbances. The probability of freak waves in the context of these simulations is also discussed. The instability is first studied for the symmetric Lorentz spectrum, and continued for the realistic asymmetric Joint North Sea Wave Project (JONSWAP) spectrum of ocean waves with variable directional spreading and steepness. It is found that instability depends on the directional spreading and parameters α and γ of the JONSWAP spectrum, where α and γ are the energy scale and the peak enhancement factor, respectively. Both influence the mean steepness of waves with such a spectrum, although in different ways. Specifically, if the instability stops as a result of the directional spreading, increase of the steepness by increasing α or γ can reactivate it. A criterion for the instability is suggested as a dimensionless 'width parameter', Π. For the unstable conditions, long-time evolution is simulated by integrating the Alber equation numerically. Recurrent evolution is obtained, which is a stochastic counterpart of the Fermi–Pasta–Ulam recurrence obtained for the cubic Schrödinger equation. This recurrence enables us to study the probability of freak waves, and the results are compared to the values given by the Rayleigh distribution. Moreover, it is found that stability–instability transition, the most unstable mode, recurrence duration and freak wave probability depend solely on the dimensionless 'width parameter', Π.

Key words: surface gravity waves, waves/free-surface flows

1. Introduction

The deterministic nonlinear evolution in time t and in space $\boldsymbol{x} = (x_1, x_2)$ of an ocean wave field with a narrow spectral band is governed by the cubic Schrödinger equation

† Email address for correspondence: ABabanin@swin.edu.au

‡ Currently on leave from the Department of Mathematics, Hasanuddin University, Makassar, Indonesia.

	Homogeneous	
Gaussian	Yes	No
Yes	Pierson (1955)	Alber (1978)
No	Longuet-Higgins (1976)	Crawford, Saffman & Yuen (1980)

TABLE 1. Various models for random ocean wave fields.

(see Zakharov 1968):

$$\mathrm{i}\left(\frac{\partial A}{\partial t} + \frac{1}{2}\sqrt{\frac{g}{k_0}}\frac{\partial A}{\partial x_1}\right) - \frac{1}{4}\sqrt{\frac{g}{k_0^3}}\left(\frac{\partial^2 A}{\partial x_1^2} - 2\frac{\partial^2 A}{\partial x_2^2}\right) = \frac{1}{2}\sqrt{gk_0^5}\,|A|^2 A, \tag{1.1}$$

where $A(\boldsymbol{x}, t)$ is the complex amplitude envelope, centred around the carrier wavenumber $\boldsymbol{k}_0 = (k_0, 0)$, and related to the free-surface elevation $\eta(\boldsymbol{x}, t)$ by

$$2\eta(\boldsymbol{x}, t) = A(\boldsymbol{x}, t)\exp[\mathrm{i}(k_0 x_1 - \sqrt{gk_0}\,t)] + *. \tag{1.2}$$

In the above and elsewhere, g is the acceleration due to gravity and $*$ stands for the complex conjugate. It is generally assumed that (1.1) and (1.2) describe the evolution also when $A(\boldsymbol{x}, t)$ and $\eta(\boldsymbol{x}, t)$ are random functions.

Indeed, Longuet-Higgins (1976) and Alber (1978) have used (1.1) as their starting point for the formulation of two rather different stochastic evolution equations. Longuet-Higgins assumed that the wave field is a homogeneous and nearly Gaussian random process; whereas Alber enabled the random process to be inhomogeneous, but required Gaussianity. To somewhat clarify the above terminology, we define the two-point space correlation function

$$\rho(\boldsymbol{x}, \boldsymbol{r}, t) = \langle A(\boldsymbol{x} + \tfrac{1}{2}\boldsymbol{r}, t)A^*(\boldsymbol{x} - \tfrac{1}{2}\boldsymbol{r}, t)\rangle, \tag{1.3}$$

where $\langle\ \rangle$ denotes the ensemble average and $\boldsymbol{r}$ is the spacing. We further mention a fourth-order average, which appears during the derivations:

$$\begin{aligned} f(\boldsymbol{x}, \boldsymbol{r}, t) = \langle &A^2(\boldsymbol{x} + \tfrac{1}{2}\boldsymbol{r}, t)A^*(\boldsymbol{x} + \tfrac{1}{2}\boldsymbol{r}, t)A^*(\boldsymbol{x} - \tfrac{1}{2}\boldsymbol{r}, t)\\ &- A^2(\boldsymbol{x} - \tfrac{1}{2}\boldsymbol{r}, t)A^*(\boldsymbol{x} - \tfrac{1}{2}\boldsymbol{r}, t)A^*(\boldsymbol{x} + \tfrac{1}{2}\boldsymbol{r}, t)\rangle. \end{aligned} \tag{1.4}$$

One should note that: (i) for a homogeneous process,

$$\rho_h = \rho_h(\boldsymbol{r}, t) \tag{1.5}$$

is independent of $\boldsymbol{x}$; and (ii) for a nearly Gaussian process, (1.4) reduces to

$$f(\boldsymbol{x}, \boldsymbol{r}, t) = 2\rho(\boldsymbol{x}, \boldsymbol{r}, t)[\rho(\boldsymbol{x} + \tfrac{1}{2}\boldsymbol{r}, \boldsymbol{0}, t) - \rho(\boldsymbol{x} - \tfrac{1}{2}\boldsymbol{r}, \boldsymbol{0}, t)] + c(\boldsymbol{x}, \boldsymbol{r}, t), \tag{1.6}$$

where $c(\boldsymbol{x}, \boldsymbol{r}, t)$ is the fourth-order cumulant, assumed to be small under the assumption of weak non-Gaussianity or zero under the assumption of strict Gaussianity. It is also important to mention that, for a homogeneous process, (1.6) becomes

$$f_h(\boldsymbol{r}, t) = c_h(\boldsymbol{r}, t), \tag{1.7}$$

which has to be estimated by using sixth-order averages and a closure given by the assumption of vanishing sixth-order cumulants. We summarize the four possibilities in table 1.

From table 1, it is clear that Crawford *et al.* (1980) provide the more general option, but their result is so cumbersome that it has so far never been used. Pierson's (1955) model turns out to be stationary also and disregards the contribution of nonlinear interactions altogether.

Longuet-Higgins's (1976) result is actually the narrow-band limit of the Hasselmann (1962) kinetic equation. So far the kinetic equation is the most frequently used in stochastic models, but its time scale is proportional to ε^{-4}, where ε is a typical small wave steepness.

Alber (1978) used his equation to study the instability of a homogeneous wave field to inhomogeneous disturbances. Alber's findings are actually the stochastic counterpart of the well-known deterministic Benjamin–Feir instability, which can be described with the cubic Schrödinger equation. The growth rates of the inhomogeneous instabilities are proportional to ε^2, reflecting the fact that the time scale of the Alber equation is proportional to ε^{-2}. Although Alber does not state it explicitly, the choice of his initial small inhomogeneous disturbances discloses a certain correlation between their phases and those of the homogeneous base state.

From the cubic Schrödinger equation, it is known that the Benjamin–Feir instability leads not to a permanent end state, but to an unsteady series of modulation and demodulation cycles, called the Fermi–Pasta–Ulam recurrence phenomenon (see Yuen & Ferguson 1978*a*,*b*; Janssen 1981; Stiassnie & Kroszynski 1982). Stiassnie, Regev & Agnon (2008) solved the Alber equation in one spatial dimension numerically and showed that a stochastic parallel to the Fermi–Pasta–Ulam recurrence exists. Their initial homogeneous wave fields have simple one-dimensional spectra of three different types: square, Lorentz and Gaussian. This stochastic recurrence enabled them to study the probability of waves that are higher than twice or three times the significant wave height, which are usually called freak waves (see Kharif & Pelinovsky 2003; Onorato *et al.* 2004; Mori *et al.* 2007). This classification is related to the work of Longuet-Higgins (1952), who showed that the wave heights in a wave field with a narrow spectrum, within the theory of linear waves, are Rayleigh-distributed. From the Rayleigh distribution one can calculate that the probabilities for waves that are higher than twice or three times the significant wave height are 3×10^{-4} and 10^{-8}, respectively. The latter is such an extremely rare event that it would require an unrealistically long period of approximately 30 years to encounter such an exceptional freak wave (Regev *et al.* 2008). Moreover, Regev *et al.* (2008) used the one-dimensional Alber equation to study the probability of freak waves initialized by a Gaussian spectrum.

The aforementioned findings are limited to unidirectional wave fields. Real sea states, however, are characterized by wave components propagating along different directions. Numerical (e.g. Onorato, Osborne & Serio 2002; Socquet-Juglard *et al.* 2005; Gramstad & Trulsen 2007; Eliasson & Shukla 2010; Toffoli *et al.* 2010*b*) and experimental (Onorato *et al.* 2009*b*; Waseda, Kinoshita & Tamura 2009) studies have revealed that wave directional spreading reduces the effect of instability and concurrently reduces the probability of occurrence of freak waves. Although for one-dimensional wave trains the qualitative features of this instability are well established (Babanin *et al.* 2010, 2011*b*), for the directional wave fields quantitative guidance exists, but is much less certain (Babanin 2011; Babanin *et al.* 2011*a*).

Based on the Alber equation, the present study shows that more realistic Joint North Sea Wave Project (JONSWAP) spectra of ocean waves with directional distributions can actually reproduce a stochastic recurrence that is parallel to Fermi–Pasta–Ulam recurrence and the conditions for its occurrence are also specified. The periodicity of the stochastic properties in space, and their recurring structure in time, render

the calculation of extreme conditions such as the occurrence of freak waves straightforward, by taking one recurrence cycle to establish the probability density function (p.d.f.) and then calculating the probability of the freak waves.

This paper is organized as follows. The mathematical formulation and background are given in §2. Linear stability analysis and long-time stochastic recurrence are discussed in §§3 and 4, respectively. The probability of freak waves is calculated in §5. The main findings are summarized and discussed in §6. More technical aspects such as the derivation of invariants of motion (which help to control the accuracy of the solutions) and the numerical approach are deferred to appendices A and B. Moreover, the details of the approximate solution of (2.4) for general spectra, which is called a 'general method', and dimensional considerations leading to the definition of the width parameter, Π, are shown in appendices C and D, respectively.

2. Formulation and background

The Alber (1978) equation for narrow-banded random surface waves on infinitely deep water can be expressed as

$$\mathrm{i}\left(\frac{\partial \rho}{\partial t} + \frac{1}{2}\sqrt{\frac{g}{k_0}}\frac{\partial \rho}{\partial x_1}\right) - \frac{1}{4}\sqrt{\frac{g}{k_0^3}}\left(\frac{\partial^2 \rho}{\partial x_1 \partial r_1} - 2\frac{\partial^2 \rho}{\partial x_2 \partial r_2}\right)$$
$$= \sqrt{gk_0^5}\,\rho(\mathbf{x},\mathbf{r},t)[\rho(\mathbf{x}+\tfrac{1}{2}\mathbf{r},\mathbf{0},t) - \rho(\mathbf{x}-\tfrac{1}{2}\mathbf{r},\mathbf{0},t)]. \quad (2.1)$$

Following Landsberg (1955), the correlation function, for a homogeneous sea, ρ_h, depends only on $\mathbf{r}$, and is related to the energy spectrum $S(\mathbf{k})$ through

$$\rho_h(\mathbf{r}) = \int_{-\infty}^{\infty} S(\mathbf{k})\exp[\mathrm{i}(\mathbf{k}-\mathbf{k}_0)\cdot\mathbf{r}]\,\mathrm{d}\mathbf{k}. \quad (2.2)$$

Note that any $\rho_h(\mathbf{r})$ is a trivial solution of the Alber equation (2.1).

In order to study the instability of homogeneous seas to inhomogeneous disturbances, we consider a solution of the form:

$$\rho(\mathbf{x},\mathbf{r},t) = \rho_h(\mathbf{r}) + \delta R(\mathbf{r})\left\{\exp\left[\mathrm{i}\left(px_1 + qx_2 - \frac{p}{2}\sqrt{\frac{g}{k_0}}\,t - \Omega t\right)\right] + *\right\}, \quad (2.3)$$

where $\delta = o(1)$ is a dimensionless inhomogeneity parameter, $R(\mathbf{0})$ is real, (p,q) is the wavenumber of the disturbance, with $p \geqslant 0$ and $q \geqslant 0$, and Ω is its frequency. To obtain instability, $\Omega^{(I)} = \mathrm{Im}\{\Omega\}$ must be positive. Substituting (2.3) into (2.1), and neglecting terms of order δ^2, leads to a linear first-order partial differential equation for $R(\mathbf{r})$, which has a straightforward solution. For $\mathbf{r} = \mathbf{0}$ this solution produces the following dispersion relation for the disturbance:

$$1 = 4k_0^4(p^2 - 2q^2)\int_{-\infty}^{\infty}\frac{S(\mathbf{k})\,\mathrm{d}\mathbf{k}}{\frac{1}{4}(p^2 - 2q^2)^2 - [p(k_1 - k_0) - 2qk_2 + 4k_0^2\Omega/\sqrt{gk_0}]^2}, \quad (2.4)$$

which is independent of the choice of $R(\mathbf{r})$.

Equation (2.3) with Ω given by (2.4) constitutes the linear stability analysis of $\rho_h(\mathbf{r})$, which by its nature is only valid for short times. Its main contribution is $(p^{(max)}, q^{(max)})$, i.e. the wavenumber of the disturbance for which the growth rate $\Omega^{(I)}$ obtains its maximum. To study the long-time evolution of the Alber equation's solutions (2.1), one needs an elaborate numerical solver in a five-dimensional space (x_1, x_2, r_1, r_2, t). The numerical method to integrate the Alber equation can be found in appendix A.

Assuming that the long-time evolution of the solution (2.3) maintains its periodicity in x, one can show that the Alber equation (2.1) has the following invariants of time:

$$I_1 = \int \rho(x, r, t)\Big|_{r=0} \, dx, \tag{2.5}$$

$$I_{21} = \int \frac{\partial \rho(x, r, t)}{\partial r_1}\Big|_{r=0} \, dx, \quad I_{22} = \int \frac{\partial \rho(x, r, t)}{\partial r_2}\Big|_{r=0} \, dx, \tag{2.6a,b}$$

$$I_3 = \int \rho^2(x, r, t)\Big|_{r=0} \, dx + \frac{1}{4k_0^4} \int \frac{\partial^2 \rho(x, r, t)}{\partial r_1^2}\Big|_{r=0} \, dx - \frac{1}{2k_0^4} \int \frac{\partial^2 \rho(x, r, t)}{\partial r_2^2}\Big|_{r=0} \, dx, \tag{2.7}$$

where all integrals in (2.5)–(2.7) are over the two-dimensional domain $x_1 \in [0, 2\pi/p]$, $x_2 \in [0, 2\pi/q]$. See appendix B for details of the derivations of these invariants.

3. Linear stability analysis

Any further progress with (2.4) requires that $S(k)$ is specified. Here, we initially study the instability of the ocean surface with symmetric Lorentz spectrum and continue with the more realistic asymmetric ocean-wave JONSWAP spectrum.

3.1. *Lorentz spectrum*

The Lorentz spectrum is given by Crawford *et al.* (1980) as

$$S(k) = S_2(k_1, k_2) = \frac{W_1 W_2 a_0^2}{2\pi^2[(k_1 - k_0)^2 + W_1^2][k_2^2 + W_2^2]}, \tag{3.1}$$

where a_0 is the wave amplitude and $a_0^2/2$ is the energy density; (W_1, W_2) are measures of the spectral width in directions parallel and perpendicular to the carrier, respectively. Substituting (3.1) into (2.4), and following Crawford *et al.* (1980), the growth rate of unstable disturbances is given by

$$\Omega_2^{(I)} = \frac{\sqrt{gk_0}}{2} \left\{ \sqrt{\left[\frac{1}{4}\left(\frac{p}{k_0}\right)^2 - \frac{1}{2}\left(\frac{q}{k_0}\right)^2\right]\left[2a_0^2 k_0^2 - \frac{1}{4}\left(\frac{p}{k_0}\right)^2 + \frac{1}{2}\left(\frac{q}{k_0}\right)^2\right]} \right.$$
$$\left. - \frac{W_1 p}{2k_0^2} - \frac{W_2 q}{k_0^2} \right\}. \tag{3.2}$$

The one-dimensional counterparts of (3.1) and (3.2) are

$$S(k) = S_1(k_1) = \frac{W_1 a_0^2}{2\pi[(k_1 - k_0)^2 + W_1^2]}, \tag{3.3a}$$

$$\Omega_1^{(I)} = \frac{p}{4}\sqrt{\frac{g}{k_0}} \left\{ \sqrt{2a_0^2 k_0^2 - \frac{1}{4}\left(\frac{p}{k_0}\right)^2} - \frac{W_1}{k_0} \right\}. \tag{3.3b}$$

From (3.3b) and the condition of instability $\Omega_1^{(I)} > 0$, one can see that (3.3a) is stable for any p, if

$$\frac{W_1}{k_0} > \sqrt{2}a_0 k_0. \tag{3.4}$$

Note that $a_0 k_0$ is the steepness of the wave with wavenumber k_0 and amplitude a_0.

The point of maximum growth rate is

$$p_1^{(max)} = k_0 \left\{ 4a_0^2 k_0^2 - \frac{1}{2}\left(\frac{W_1}{k_0}\right)^2 - \frac{W_1}{2k_0}\sqrt{16a_0^2 k_0^2 + \left(\frac{W_1}{k_0}\right)^2} \right\}^{1/2}, \qquad (3.5a)$$

and the maximum growth rate itself is

$$\Omega_1^{(max)} = \Omega_1^{(I)}(p_1^{(max)}) = \frac{p_1^{(max)}}{4}\sqrt{\frac{g}{k_0}}\left\{ \sqrt{2a_0^2 k_0^2 - \frac{1}{4}\left(\frac{p_1^{(max)}}{k_0}\right)^2} - \frac{W_1}{k_0} \right\}. \quad (3.5b)$$

For the two-dimensional Lorentz spectrum (3.1), one can prove that the most unstable mode is

$$(p_2^{(max)}, q_2^{(max)}) = (p_1^{(max)}, 0) \qquad (3.6a)$$

and that its growth rate is

$$\Omega_2^{(max)} = \Omega_1^{(max)}, \qquad (3.6b)$$

independent of W_2.

The special features of the Lorentz spectrum (3.1) are its symmetry and the fact that it enables integration of (2.4) analytically.

3.2. *Unidirectional JONSWAP spectrum*

A unidirectional JONSWAP spectrum as a function of wavenumber (see Komen *et al.* 1994; Holthuijsen 2007) is given by

$$S(k_1) = \frac{\alpha}{2k_1^3}\exp\left(\frac{-5k_0^2}{4k_1^2}\right)\gamma^{\exp\left[-\left(\sqrt{k_1}-\sqrt{k_0}\right)^2/2\sigma^2 k_0\right]}, \qquad (3.7a)$$

where γ and α are the peak enhancement factor and the energy scale of the spectrum, respectively, and $\sigma = 0.08$ defines the peak width. For the total energy density of any spectrum, we have (Dysthe *et al.* 2003; Stiassnie *et al.* 2008)

$$a_0^2/2 \equiv (\varepsilon/k_0)^2/2 \equiv \int S(k)\,\mathrm{d}k. \qquad (3.7b)$$

In order to find the maximum growth rate and the point of maximum growth of this spectrum, (3.7a) is substituted into (2.4). However, since (2.4) cannot be solved analytically for the JONSWAP spectrum, it is necessary to seek an approximate solution. To this end, we replace the original spectrum by a sum of weighted Dirac functions and replace (2.4) by a high-order (up to 70) algebraic equation, seeking the root with the largest imaginary contribution. The details of this rather 'general method' can be found in appendix C. Moreover, its validity is demonstrated in figure 1 using the Lorentz spectrum, in which the analytical expressions (3.5a) and (3.5b), given by the solid line, are compared with the approximate results obtained by the 'general method' and marked by dots. The results in figure 1 are given in dimensionless variables, where $\varepsilon = a_0 k_0$ is the steepness, $\tilde{W}_1 = W_1/\varepsilon k_0$, $\tilde{P}_1^{(max)} = p_1^{(max)}/\varepsilon k_0$ and $\tilde{\Omega}_1^{(max)} = \Omega_1^{(max)}/\varepsilon^2\sqrt{gk_0}$. We have to emphasize that the main difference between the JONSWAP spectrum (3.7a) and the Lorentz spectrum (3.3a) is that for the Lorentz spectrum one can integrate (2.4) analytically whereas for the JONSWAP spectrum one cannot.
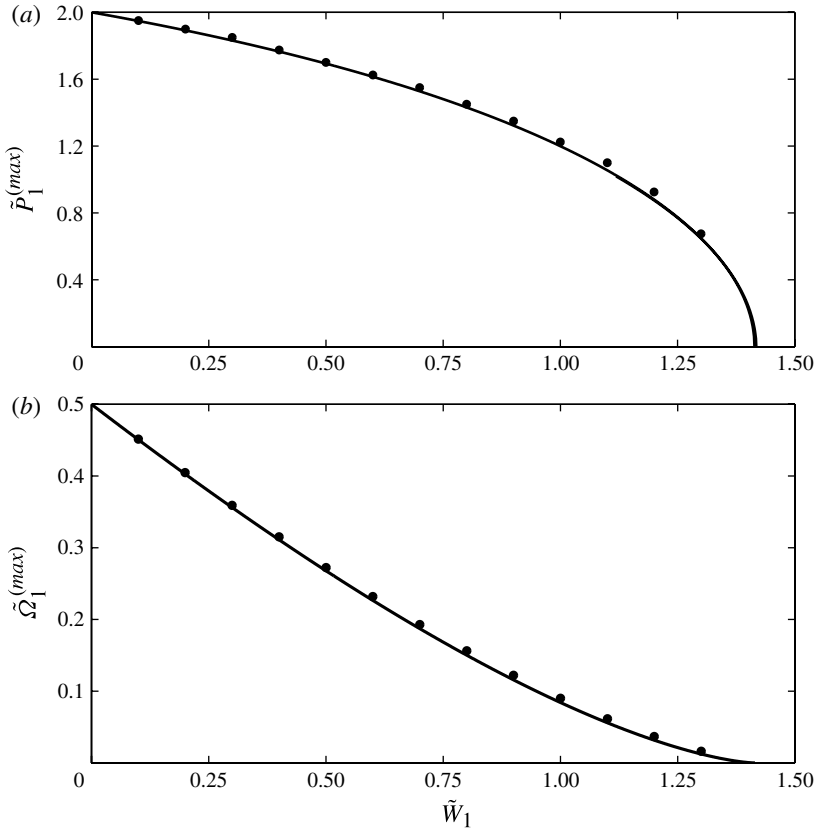
FIGURE 1. Validation of the 'general method' (● ● ●) against the analytical solution (——) for a Lorentz spectrum: (*a*) most unstable mode and (*b*) its growth rate.

For a JONSWAP spectrum, simple dimensional analysis considerations by applying the Buckingham theorem (Buckingham 1914) led us to the conclusions that $\tilde{P}_1^{(max)} = p_1^{(max)}/\varepsilon k_0$ and $\tilde{\Omega}_1^{(max)} = \Omega_1^{(max)}/\varepsilon^2\sqrt{gk_0}$ are functions of a dimensionless 'width parameter'

$$\Pi_1 = \frac{\varepsilon}{\alpha\gamma}. \tag{3.8}$$

The details of the dimensional analysis approach, which was inspired by the Benjamin–Feir index (BFI) as introduced by Onorato *et al.* (2001) and Janssen (2003), can be found in appendix D. It has to be mentioned that our dimensionless width parameter shows the detailed meaning of the ratio of wave steepness to wave bandwidth in the spectral context.

The width parameter Π_1 is related to BFI, but is not another form of BFI. The latter had been introduced for quasi-monochromatic wave trains, being the ratio of steepness to bandwidth, which are unambiguous properties in such trains. They are not unambiguous for wave fields with continuous spectrum.

In a JONSWAP spectrum, both α and γ are connected with both steepness and bandwidth. Moreover, neither of them is constant in evolving wave spectra and, even

on average, any change to α is accompanied by a change to γ (e.g. Babanin & Soloviev 1998*a*; Onorato *et al.* 2003).

For the spectrum of ocean waves, the JONSWAP spectrum being the most popular parametrization, the same steepness can be achieved either by varying α and keeping γ constant, or vice versa. This same steepness, therefore, has different implications for the spectral bandwidth and for modulational instability. If we increase α, then to keep the steepness constant we should decrease γ. This means that spectra become broader and this leads to corresponding implications for the instability of nonlinear groups – i.e. the growth rates of most unstable modes are expected to decrease or even be suppressed. If we increase γ, then to keep the steepness constant we should decrease α. Such a combination will instigate rapid narrowing of the spectral bandwidth of dominant waves, which we expect to be associated with their instability, and which is the most important outcome in the practical sense, e.g. for wave breaking or freak wave probability.

Thus, separation of the relative contributions of α and γ into the total steepness and the characteristic bandwidth of waves with continuous spectrum identify important physical differences between wave fields with full spectrum and quasi-monochromatic wave trains. It does not deny the previous analogies in terms of BFI, but expands them and is an important new contribution of this paper.

Figure 2 shows $\tilde{P}_1^{(max)}$ and $\tilde{\Omega}_1^{(max)}$ as functions of Π_1 obtained for the unidirectional JONSWAP spectrum by using the 'general method' (marked by dots), as well as the best linear fit (for $\tilde{P}_1^{(max)}$ and $\tilde{\Omega}_1^{(max)}$).

The equations for the straight lines in figure 2 are

$$\tilde{P}_1^{(max)} = 2.313 - 0.976\,\Pi_1, \tag{3.9a}$$

$$\tilde{\Omega}_1^{(max)} = 0.572 - 0.557\,\Pi_1. \tag{3.9b}$$

From (3.9*b*) it is clearly seen that JONSWAP spectra are stable to inhomogeneous disturbance when $\Pi_1 > 1$, because for this condition $\tilde{\Omega}_1^{(max)}$ is negative.

3.3. *JONSWAP spectrum with a directional distribution*

Directional wave fields can be conveniently represented by a JONSWAP spectrum (3.7*a*) multiplied by the directional spreading $D(\theta) = A_d \cos^n\theta$, $|\theta| \leqslant \pi/2$, where θ is the angle of the directional distribution. Here, A_d is the inverse normalized directional spectral width, which was defined according to Babanin & Soloviev (1987, 1998*b*) as

$$A_d(f)^{-1} = \int_{-\pi}^{\pi} K(f,\theta)\,\mathrm{d}\theta, \tag{3.10a}$$

where $K(f,\theta)$ is the normalized directional spectrum

$$K(f,\theta_{max}) = 1, \tag{3.10b}$$

i.e. higher values of A_d correspond to narrower directional distributions. The inverse width A_d is a convenient property to use as a proxy of the directional spread because there is an extensive parametrization available for its dependences (Babanin & Soloviev 1987, 1998*b*) and it is unambiguously analytically connected with other existing directional-spread characteristics used in the literature, even for bimodal directional spectra. For example, for the normalized spectrum $K(f,\theta) = \cos^{n(f)}(\theta - \theta_{max})$, this analytical connection is

$$A_d = \frac{\Gamma(1 + 0.5n)}{\sqrt{\pi}\,\Gamma(0.5 + 0.5n)}, \tag{3.11a}$$
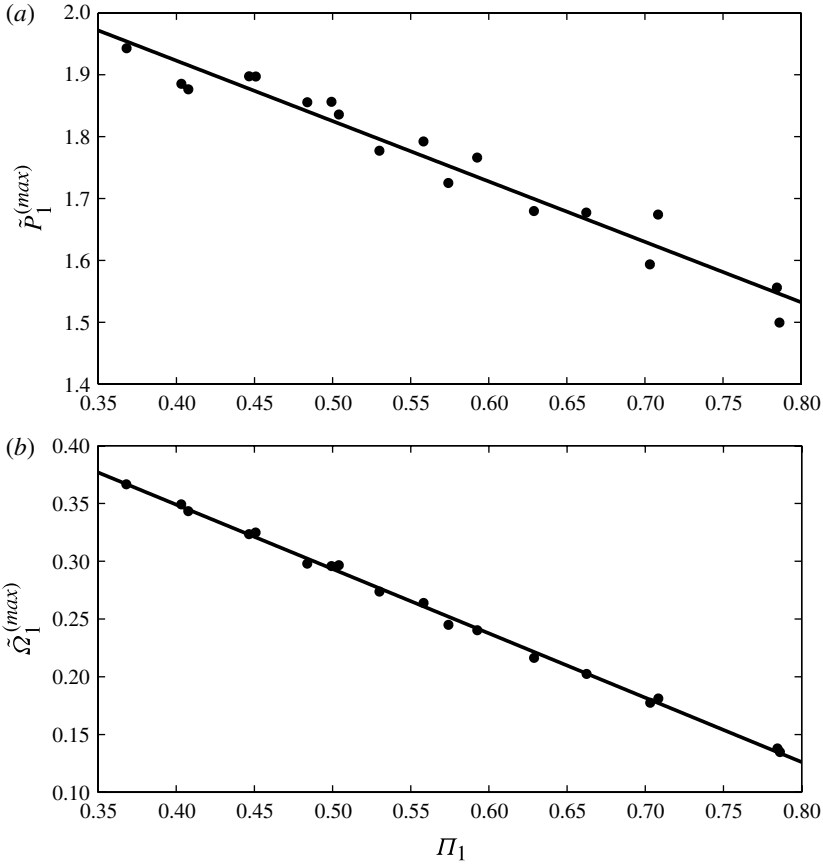
FIGURE 2. Results of linear stability analysis for unidirectional JONSWAP spectra as a function of the 'width parameter' Π_1: (*a*) most unstable mode and (*b*) its growth rate.

and transformed into the wave vector plane (k_1, k_2), the JONSWAP spectrum with such directional distribution is

$$S(\boldsymbol{k}) = \frac{\alpha A_d k_1^n}{2\left(k_1^2 + k_2^2\right)^{2+0.5n}} \exp\left(\frac{-5k_0^2}{4(k_1^2+k_2^2)}\right) \gamma^{\exp\left[\frac{-1}{2\sigma^2}\left(\frac{(k_1^2+k_2^2)^{0.25}}{k_0^{0.5}}-1\right)^2\right]}.$$

(3.11*b*)

Moreover, this spectrum is a function of four parameters, k_0, α, γ and n, which are the carrier wavenumber, the energy scale, the peak enhancement factor and the degree of the directional spreading, respectively; where, the higher the value of n, the narrower the spectrum. Note that A_d and n are unambiguously connected through (3.11*a*).

Furthermore, we assume without loss of generality that the maximum growth rate occurs for $q = 0$, for any narrow spectrum with carrier $(k_0, 0)$; see (3.6*a*). This assumption simplifies (2.4), as well as (2.1), substantially. Following a similar procedure to that outlined in the previous section, we obtained that, for the JONSWAP spectrum with a directional distribution, $\tilde{P}_2^{(max)} = p_2^{(max)}/\varepsilon k_0$ and $\tilde{\Omega}_2^{(max)} = \Omega_2^{(max)}/\varepsilon^2\sqrt{gk_0}$ are functions of a slightly corrected dimensionless

'width parameter',

$$\Pi_2 = \frac{\varepsilon}{\alpha\gamma} + \frac{\beta}{\varepsilon A_d} \quad \text{with } \beta \ll 1. \tag{3.12}$$

Note that $(\varepsilon/\alpha\gamma)$ and $(1/\varepsilon A_d)$ are the dimensionless scaled widths in the peak direction and the transverse direction, respectively (see appendix D for the details of these dimensionless 'width parameters'). The corrected width parameter Π_2 is a convenient measure to use, owing to the fact that the directional property A_d employed by the Π_2 formulation, as well as the parameters of the JONSWAP spectrum, are characteristics of the wave directional spectrum well established experimentally and in field observations. Comprehensive parametrizations for this property are available for the wave spectrum and at all stages of wave development (Babanin & Soloviev 1987, 1998b), and therefore at any stage Π_2 can be expressed through both observation-based one-dimensional wave spectra and directional wave spectra.

Other versions of the parameter, which define the transition from the stable to unstable conditions for two-dimensional wave fields, are also available. Babanin *et al.* (2010) introduced 'directional BFI' in the same spectral terms as Π_2 here and extensively used it for investigations, tested and quantified experimentally (Babanin *et al.* 2011a,b). Another version of BFI that includes the directional effect has been introduced by Mori, Onorato & Janssen (2011) as

$$\text{BFI}_{2D} = \frac{\varepsilon}{\sqrt{\delta_\omega^2 + \frac{1}{2}\alpha_2\delta_\theta^2}}, \tag{3.13}$$

where ε, δ_ω and δ_θ are the steepness, frequency bandwidth and directional bandwidth, respectively, while α_2 is a constant.

Figure 3 gives $\tilde{P}_2^{(max)}$ and $\tilde{\Omega}_2^{(max)}$ as functions of Π_2 for about 120 different combinations of ε, α, γ and n (marked by dots), as well as the best linear fit (for $\tilde{P}_2^{(max)}$ and $\tilde{\Omega}_2^{(max)}$), which gave $\beta = 0.0256$. The equations for the straight lines in figure 3 are

$$\tilde{P}_2^{(max)} = 2.355 - 0.974\,\Pi_2, \tag{3.14a}$$

$$\tilde{\Omega}_2^{(max)} = 0.571 - 0.516\,\Pi_2. \tag{3.14b}$$

From (3.14b) it becomes clear that JONSWAP spectra with directional distributions are stable to inhomogeneous disturbance when $\Pi_2 > 1.1$ because for this condition $\tilde{\Omega}_2^{(max)}$ is negative.

It appears that the conclusion from two-dimensional Lorentz spectra is different from the conclusion obtained based on JONSWAP spectra with directional distributions in terms of dependence on the transverse width of the spectrum. However, one can easily compare these spectra, namely Lorentz spectra and JONSWAP spectra, by maintaining that the two spectra have the same total energy and momentum. One will find that changing the power of the directional distribution of JONSWAP spectra will change not only the spectral width that is perpendicular to the carrier wave of the Lorentz spectra, but also the spectral width that is parallel to the carrier wave.

4. Stochastic recurrence

4.1. *Recurrence for unidirectional JONSWAP spectrum*

The stochastic counterpart of the Fermi–Pasta–Ulam recurrence is studied by integrating the Alber equation numerically (see details of the numerical scheme in
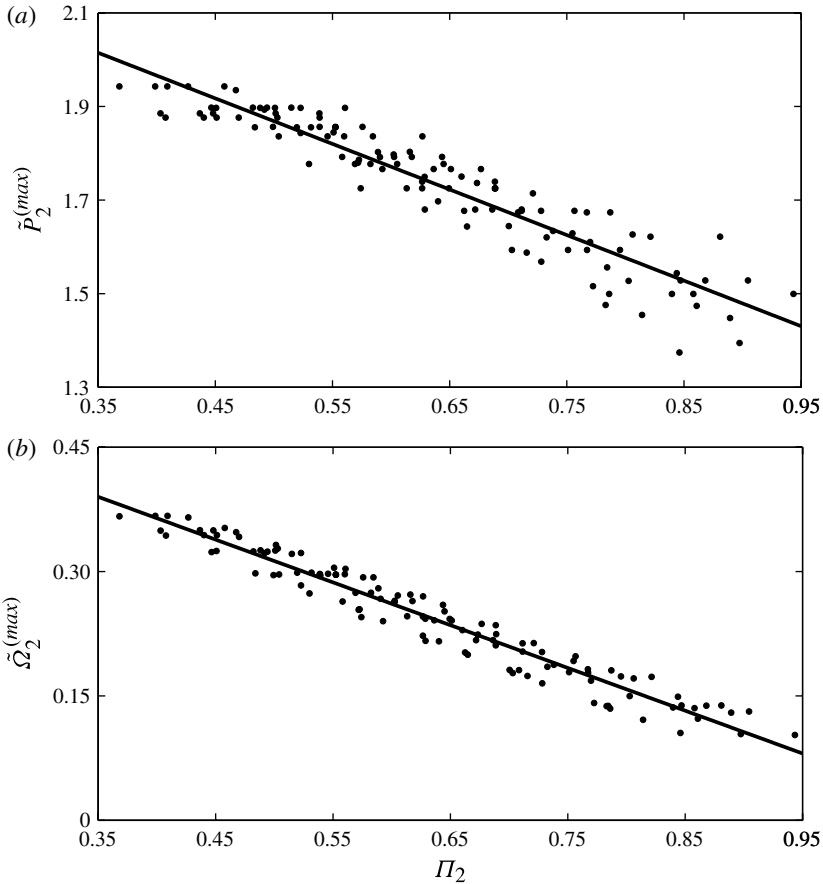
FIGURE 3. Results of linear stability analysis for JONSWAP spectra with directional distributions as a function of the 'width parameter' Π_2: (*a*) most unstable mode and (*b*) its growth rate.

appendix A). In order to apply the numerical scheme given in (A 5), the initial value of $\tilde{\rho} = k_0^2 \rho / \varepsilon^2$ must be given. This initial condition is set by (2.3) and there are some degrees of freedom, namely, the value of the inhomogeneous disturbance wavenumber $\tilde{P} = p / \varepsilon k_0$, the inhomogeneity parameter δ, and the decay $\tilde{R}(\tilde{r}_1)$. In all our examples, we take $\delta = 0.1$, $\tilde{R}(\tilde{r}_1) = \tilde{\rho}_h(\tilde{r}_1) = k_0^2 \rho_h(r_1) / \varepsilon^2$ as in (2.2) and $\tilde{P}_1^{(max)} = p_1^{(max)} / \varepsilon k_0$ is chosen from the most unstable mode for the unidirectional JONSWAP spectrum. Note that, for some different choices of $\tilde{P} = p / \varepsilon k_0$, one can refer to the work of Stiassnie *et al.* (2008). In addition, as seen from (2.2), in order to obtain $\tilde{\rho}_h(\tilde{r}_1) = k_0^2 \rho_h(r_1) / \varepsilon^2$, one has to define a spectrum, and in this case we use a unidirectional JONSWAP spectrum. However, since (2.2) cannot be integrated analytically for the JONSWAP spectrum, we, again, replace the spectrum by a sum of weighted Dirac functions. Moreover, using such spectra, one has to solve the Alber equation only in three-dimensional space (x_1, r_1, t), as some of the variables in (2.1) vanish automatically, which reduces the required computation resources significantly. As shown in § 3, a unidirectional JONSWAP spectrum is unstable for 'width parameter' $\Pi_1 < 1$. Therefore, we will choose the values of the parameters
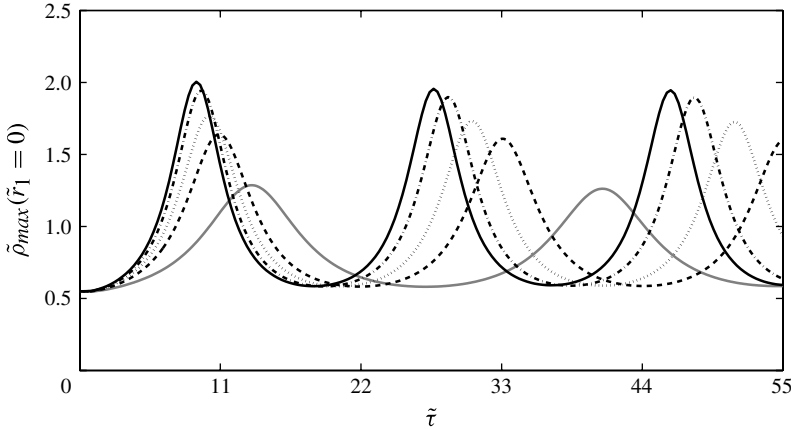
FIGURE 4. Recurrence for unidirectional JONSWAP spectra with $\gamma = 20$. Cases (see table 2): A, —; B, - -; C, ·····; D, -·-; E, —.

Case	α	γ	ε	Π_1 (3.8)	$\tilde{P}_1^{(max)}$ (3.9a)	$2\pi/\tilde{\Omega}_1^{(max)}$ (3.9b)	Numerical recurrence time	Peak enhancement
A	0.010	20	0.13	0.65	1.68	30	27	2.3
B	0.016	20	0.16	0.50	1.83	22	22	3.0
C	0.020	20	0.18	0.45	1.87	20	20	3.2
D	0.025	20	0.20	0.40	1.92	18	19	3.5
E	0.030	20	0.22	0.37	1.95	17	18	3.6
B_1	0.016	10	0.13	0.81	1.52	52	37	1.8
B_2	0.020	10	0.14	0.70	1.63	35	33	2.0
B_3	0.025	10	0.16	0.64	1.69	29	28	2.3
B_4	0.030	10	0.18	0.60	1.73	26	26	2.6

TABLE 2. Spectral parameters and evolution features for unidirectional JONSWAP spectra.

of the unidirectional JONSWAP spectra, namely α and γ, so that this condition is satisfied. To this end, we choose the initial spectra (3.7a), where $\gamma = 20$, $\sigma = 0.08$ and various values of $\alpha = 0.01, 0.016, 0.02, 0.025, 0.03$. Note that all of these cases have the same peak wavenumber of the JONSWAP spectra, that is, $k_0 = 1$.

The results of all these five different unidirectional JONSWAP spectra are shown in figure 4. Note that $\tilde{\rho}_{max}(\tilde{r}_1 = 0)$ signifies the maximum values of $k_0^2 \rho(r_1 = 0)/\varepsilon^2$ within the interval $\tilde{x}_1 \in (0, 2\pi/\tilde{P}_1^{(max)})$. Here it is plotted as a function of $\tilde{\tau} = (\varepsilon^2 \sqrt{gk_0})t$. The main features of the evolution are summarized in table 2.

From figure 4 and table 2, it is clear that the decrease in the 'width parameter' Π_1 is accompanied by an increase in the peak enhancement and a decrease in the numerical recurrence duration. In addition, the narrower the spectrum, the higher its maximum growth rate. Therefore, from all five cases, case E has the highest maximum growth rate while case A has the lowest maximum growth rate. This is also consistent with figure 4, where case E has the highest maximum correlation function evaluated at $\tilde{r}_1 = 0$. A more general picture of the values of $\tilde{\rho}(\tilde{x}_1, 0, \tilde{\tau})$ is given in figure 5. It is clearly seen from the figure that the maximum values are at $\tilde{x}_1 = 0$ and $\tilde{x}_1 = 2\pi/\tilde{P}_1^{(max)}$.
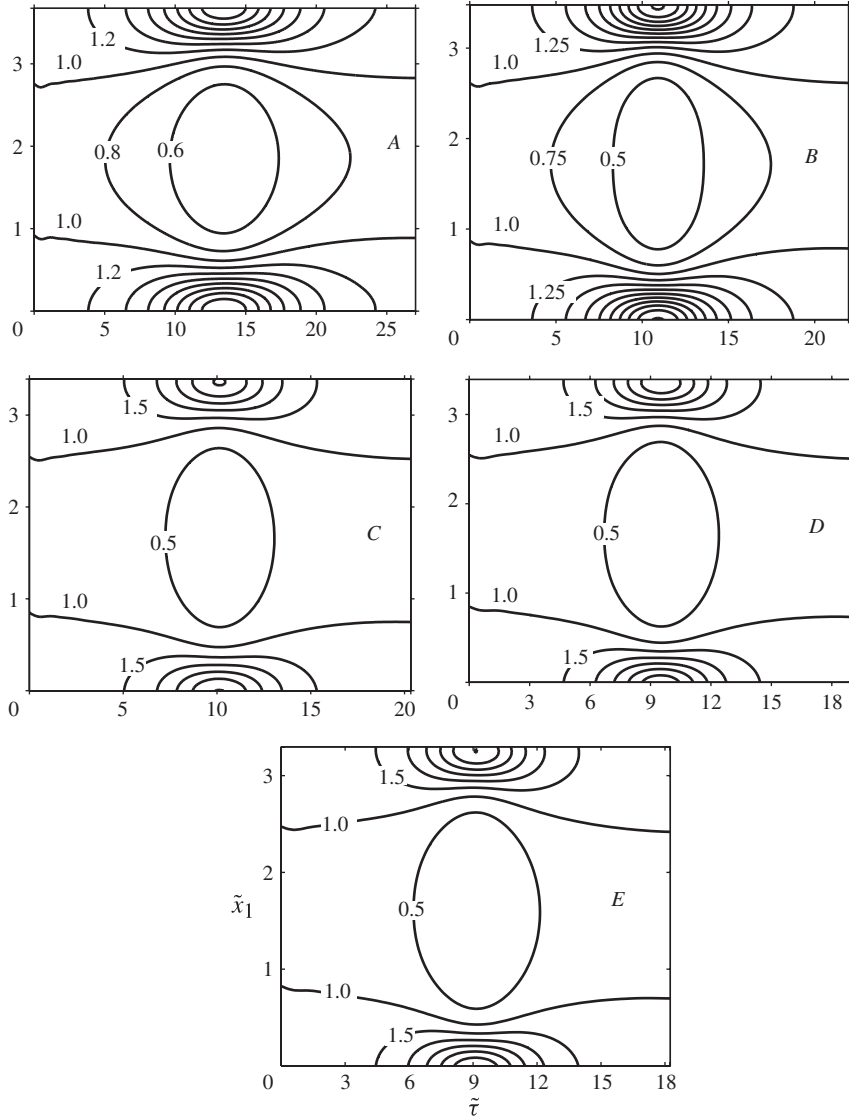
FIGURE 5. Isolines of $\tilde{\rho}(\tilde{x}_1, 0, \tilde{\tau})/\tilde{\rho}_h(0)$. Each case refers to table 2.

Changing the peak enhancement of the unidirectional JONSWAP spectrum from $\gamma = 20$ to $\gamma = 10$ and following a similar procedure to the previous case, while keeping the same energy scale for four cases, gives the stochastic recurrence as shown in figure 6. All of the features of figure 6 are similar to those of figure 4 and are summarized in table 2. For instance, the decrease in the 'width parameter' Π_1 is accompanied by an increase in the peak enhancement and a decrease in the numerical recurrence duration. Moreover, identical dimensionless 'width parameter' Π_1 gives the same maximum growth, the same point of maximum, as well as the same peak enhancement of the recurrence. Furthermore, a more general picture of the values of $\tilde{\rho}(\tilde{x}_1, 0, \tilde{\tau})$ is given in figure 7. It is clearly seen there that the maximum values are at $\tilde{x}_1 = 0$ and $\tilde{x}_1 = 2\pi/\tilde{P}_1^{(max)}$, which is similar to figure 5. In addition, looking at
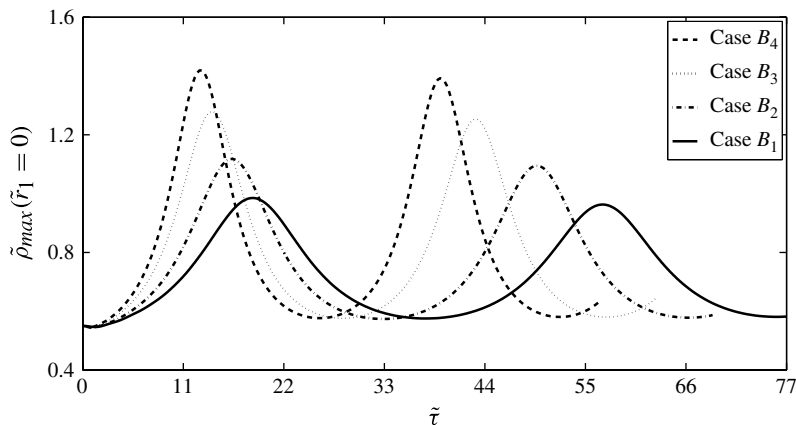
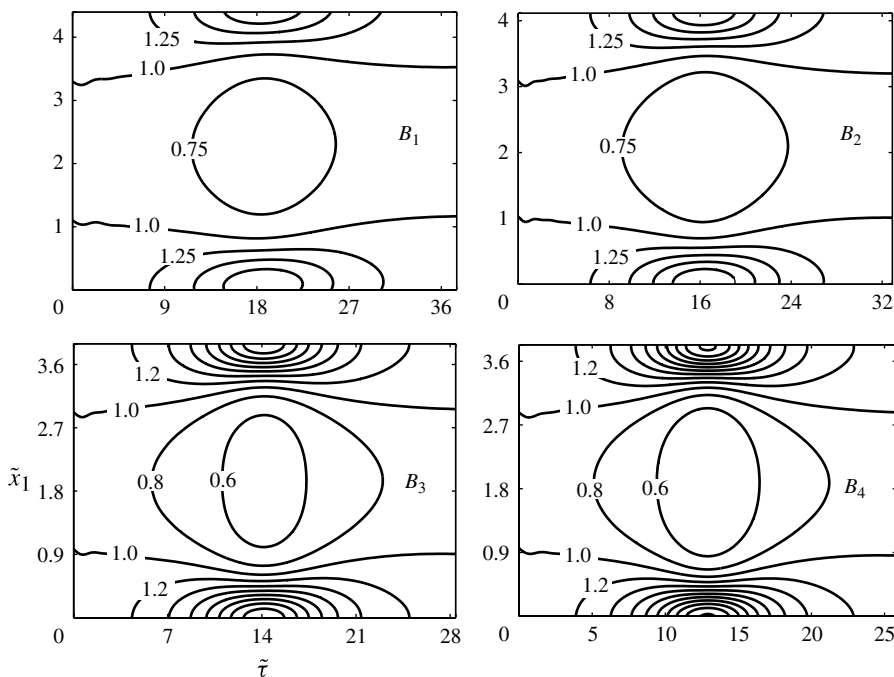FIGURE 6. Recurrence for unidirectional JONSWAP spectra with $\gamma = 10$ (see table 2).

FIGURE 7. Isolines of $\tilde{\rho}(\tilde{x}_1, 0, \tilde{\tau})/\tilde{\rho}_h(0)$. Each case refers to table 2 for $\gamma = 10$.

the case A from figure 5 and case B_3 in figure 7, one can see that they are almost the same. This is apparently because the two cases have almost the same value of the dimensionless 'width parameter' Π_1.

Now, as has been mentioned in the introduction, real sea states are not unidirectional but are characterized by wave components propagating along different directions. In the following section, these kinds of waves will be studied by including different directional distributions.
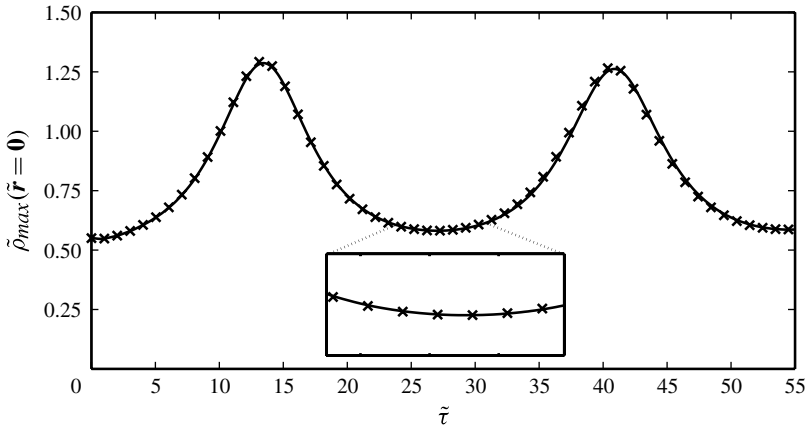
FIGURE 8. Comparison between the solution for unidirectional JONSWAP spectrum (——) and a JONSWAP spectrum with degree of directional distribution $n = 90$ (× × ×). Both spectra have the same $\gamma = 20$ and $\varepsilon = 0.13$ ($\alpha = 0.01$). The inset shows a segment at higher resolution.

4.2. *Recurrence for JONSWAP spectrum with a directional distribution*

Here we show that, whenever the 'width parameter' $\Pi_2 < 1.1$, the Alber equation yields recurring solutions. Again, in all our calculations, we take $\delta = 0.1$ and $R(\boldsymbol{r}) = \rho_h(\boldsymbol{r})$. Moreover, for the JONSWAP spectrum with a directional distribution, one has to solve the Alber equation (2.1) in a four-dimensional domain (x_1, r_1, r_2, t), which requires substantial computing resources. Furthermore, the main purpose of this section is to show the influence of the directional spreading on the long-time evolution, where the degrees of the directional distributions are $n = 90$, 50, 10 and 2, ranging from fairly narrow to very broad directional distributions. Note, however, that for practical purposes it is important to show that the results for the initial unidirectional JONSWAP spectrum as given in (3.7a) with $\gamma = 20$, $\varepsilon = 0.13$ ($\alpha = 0.01$) and $k_0 = 1$ are identical to those of a JONSWAP spectrum as given in (3.11b) with the same values of parameters and a degree of directional spreading $n = 90$. The results of these two cases are shown in figure 8. As one can see, they are hardly distinguishable.

Now, in order to show the influence of the directional spreading on the long-time evolution, we use the initial spectra as in (3.11b), which share the same values of $\gamma = 10$, $\varepsilon = 0.126$, $\alpha = 0.016$. The spectra only differ in their angular spread, having $n = 2$, 10, 50, and thus the normalization factor as given in (3.11a) is $A_d = 0.64$, 1.29 and 2.84, respectively. Moreover, their 'width parameters', as calculated from (3.12) with $\beta = 0.0256$, are $\Pi_2 = 1.11$, 0.95 and 0.86, respectively. Note that case A_3 is stable (see (3.14a)) and therefore the chosen disturbance $\tilde{P}_2^{(max)}$ does not have any particular physical meaning.

The results are shown in figure 9 for $\tilde{\rho}_{max}(\tilde{\boldsymbol{r}} = \boldsymbol{0})$, which signifies the maximum values of $k_0^2 \rho(\boldsymbol{r} = \boldsymbol{0})/\varepsilon^2$ within the interval $\tilde{x}_1 \in (0, 2\pi/\tilde{P}_2^{(max)})$, as a function of $\tilde{\tau} = \varepsilon^2 \sqrt{gk_0} \, t$.

As can be seen from figure 9, it clearly demonstrates the recurrent nature of the solution for the degree of directional spreading $n = 10$ and 50, which is from fairly broad directional spread to fairly narrow directional spread. This is in sharp contrast to the solution for $n = 2$, which describes a very broad directional spread. Note the
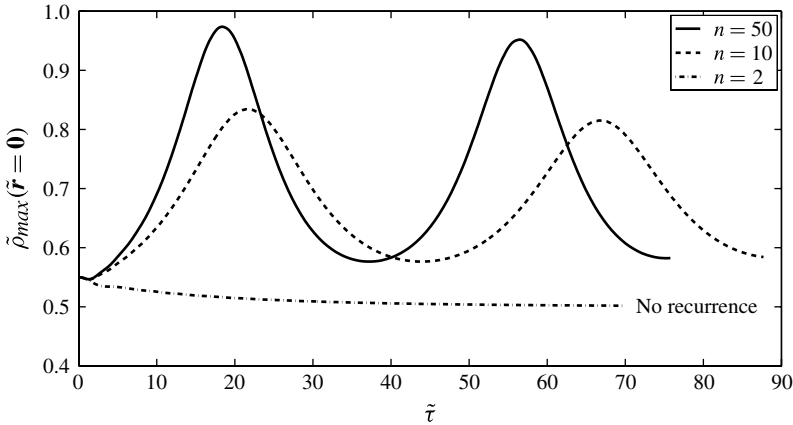
FIGURE 9. The influence of the directional spread on the variation of the maximum value of $\tilde{\rho}$ at $\tilde{r} = 0$, as a function of non-dimensional time.

Case	n	A_d	Π_2 (3.12)	$\tilde{P}_2^{(max)}$ (3.14a)	$2\pi/\tilde{\Omega}_2^{(max)}$ (3.14b)	Numerical recurrence time	Peak enhancement
A_1	50	2.84	0.86	1.52	49	37	1.77
A_2	10	1.29	0.95	1.43	75	44	1.52
A_3	2	0.64	1.11	1.28♣	—	—	—

TABLE 3. Spectral parameters and evolution features for JONSWAP spectra with three different degrees of the directional distributions n, and $\alpha = 0.016$, $\gamma = 10$, $\varepsilon = 0.126$. Here A_d is the normalization factor. *Note:* ♣ indicates the stable condition.

increase of the peak value and the shortening of the recurrence duration as a result of the decrease in Π_2 (see table 3).

A more general picture of the $\tilde{\rho}(\tilde{x}_1, 0, \tilde{\tau})$ values is given in figure 10. In these plots the values were shifted along the $\tilde{x}_1$ axis so that the maximum values are at $\tilde{x}_1 = 0$ and $\tilde{x}_1 = 2\pi/\tilde{P}_2^{(max)}$. The curves were also slightly smoothed.

Features of the long-time evolution for JONSWAP spectra with directional distributions are summarized in table 3. Moreover, as seen from table 3, the narrower the directional distribution, the smaller the value of Π_2. This implies that the narrower the directional spectrum, the more unstable the wave train is. Looking at tables 2 and 3, one can see that the discrepancy between the numerical recurrence time and $2\pi/\tilde{\Omega}_2^{(max)}$ increases with increase of Π_2.

5. The probability of freak waves

Regev *et al.* (2008) reported that freak waves may be an essentially inhomogeneous phenomenon. They occur at isolated places and times. Thus it is of interest to study their statistics using a model for inhomogeneous seas, i.e. the Alber equation in our case. As shown in the previous section, the stochastic recurrence enables us to study the probability of freak waves. This is because the stochastic recurrence can be used
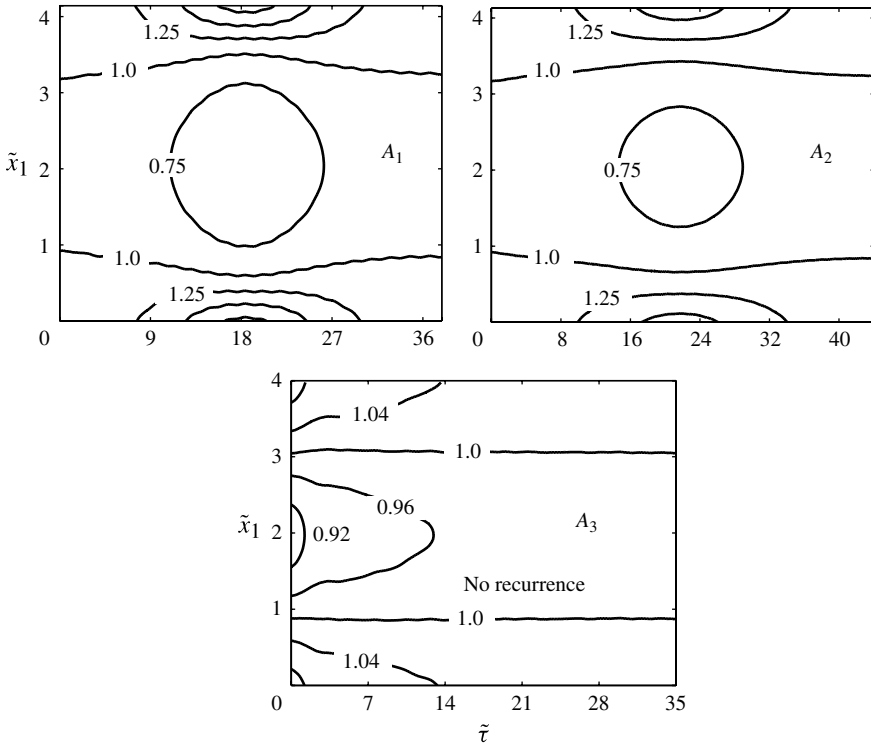
FIGURE 10. Isolines of $\tilde{\rho}(\tilde{x}_1, \mathbf{0}, \tilde{\tau})/\tilde{\rho}_h(\mathbf{0})$. Each case refers to figure 9.

to establish the p.d.f. and then to determine the probability of freak waves in a straightforward fashion. Therefore, following a procedure similar to that in Regev *et al.* (2008), one ends up with the following equation for the wave height probability:

$$P(H/H_{rms0} \geqslant \hat{H}/H_{rms0}) = \int \text{p.d.f.} \left(\frac{\tilde{\rho}}{\tilde{\rho}_h} \right) \exp \left[-\left(\frac{\hat{H}}{H_{rms0}} \right)^2 \left(\frac{\tilde{\rho}_h}{\tilde{\rho}} \right) \right] \, \text{d} \left(\frac{\tilde{\rho}}{\tilde{\rho}_h} \right), \quad (5.1)$$

where p.d.f.$(\tilde{\rho}/\tilde{\rho}_h)$ stands for the p.d.f. of $\tilde{\rho}(\tilde{x}_1, \tilde{\mathbf{r}}_1 = \mathbf{0}, \tilde{\tau})/\tilde{\rho}_h$ and H_{rms0} is the r.m.s. wave height of the homogeneous sea where $H_{rms0}^2 \propto \rho_h(\mathbf{r} = \mathbf{0}) = \int S(\mathbf{k}) \, \text{d}\mathbf{k}$. Therefore, in order to apply (5.1), one needs to calculate the p.d.f. of $\tilde{\rho}/\tilde{\rho}_h$, which will be shown in the following sections. Moreover, in the following two sections, we will show the probability of freak waves for unidirectional JONSWAP spectra and JONSWAP spectra with directional distributions.

5.1. *Unidirectional JONSWAP spectrum*

In order to find the probability function, p.d.f.$(\tilde{\rho}/\tilde{\rho}_h)$, again, we adopted the method used in Regev *et al.* (2008). First, more than 100 locations evenly distributed along the $\tilde{x}_1$ axis from 0 to $2\pi/\tilde{P}_1^{(max)}$ were taken. Over one recurrence cycle (see figure 4), $\tilde{\rho}/\tilde{\rho}_h$ was sampled at 100 evenly distributed sampling times, so that more than 10 000 values of $\tilde{\rho}(\tilde{x}_1, 0, \tilde{\tau})/\tilde{\rho}_h(0)$ were used to establish p.d.f.$(\tilde{\rho}/\tilde{\rho}_h)$. The isolines of these $\tilde{\rho}/\tilde{\rho}_h$ are plotted in figure 5 for the above-mentioned five different cases (table 2).

Second, all of the values were arranged from the lowest to the highest and divided into 100 evenly spaced increments in $\tilde{\rho}/\tilde{\rho}_h$, for example, from 0.26 to 4 for $\gamma = 20$
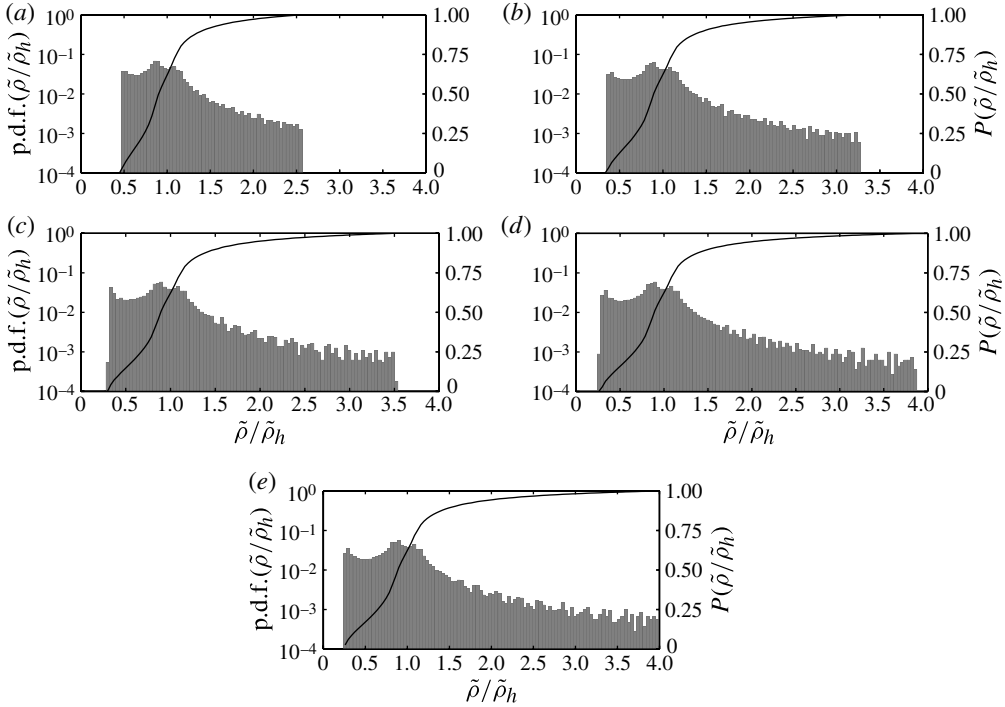
FIGURE 11. Probability density function p.d.f.$(\tilde{\rho}/\tilde{\rho}_h)$ (histogram) and probability function $P(\tilde{\rho}/\tilde{\rho}_h)$ (solid line) as functions of $\tilde{\rho}/\tilde{\rho}_h$: (*a*)–(*e*) cases *A*–*E*, respectively.

and from 0.5 to 2.8 for $\gamma = 10$. The probability of each increment was calculated as the number of elements within the increment divided by the total number of values used. Figure 11 presents the p.d.f. of $\tilde{\rho}/\tilde{\rho}_h$ by a bar diagram (to ease comparison, the widths of the bins in all bar diagrams are equal) and the probability function (the probability of obtaining a value smaller than or equal to $\tilde{\rho}/\tilde{\rho}_h$) is given by the solid line for the five different cases. From figures 5 and 11 one can see that, for cases *D* and *E*, many bins are activated and that the number of active bins reduces when the 'width parameter' Π_1 increases as shown in table 2.

The probability function for the wave height given by (5.1) is calculated on the basis of the known values of p.d.f.$(\tilde{\rho}/\tilde{\rho}_h)$ as shown in figure 11. In figure 12, these wave-height probabilities for inhomogeneous seas are then compared with the probability obtained for the homogeneous sea according to the Rayleigh distribution, as in equation (8) of Regev *et al.* (2008) or equation (3.5) of Young (1999). In the figure, probability values of freak waves, that is, the probability for waves with $\hat{H} \geqslant 2.84 H_{rms0}$ (i.e. $\hat{H} \geqslant 2H_s$), is plotted (note that our H_{rms0} and significant wave height H_s are connected as $H_s = \sqrt{2} H_{rms0}$). For reference, the inset shows full comparison (starting from zero wave height) between the probability of the homogeneous sea and the probability obtained from the Alber equation for case *E*. As can be seen from the inset, the probability up to $\hat{H} \geqslant 1.46 H_{rms0}$ is greater for the Rayleigh distribution, but after the intersection point the probability is greater for the results obtained from the Alber equation. For other cases, namely for cases *A*, *B*, *C* and *D*, one can obtain that the intersection values are in the range $\hat{H}/H_{rms0} \in (1.46, 1.53)$. In addition, as one can see
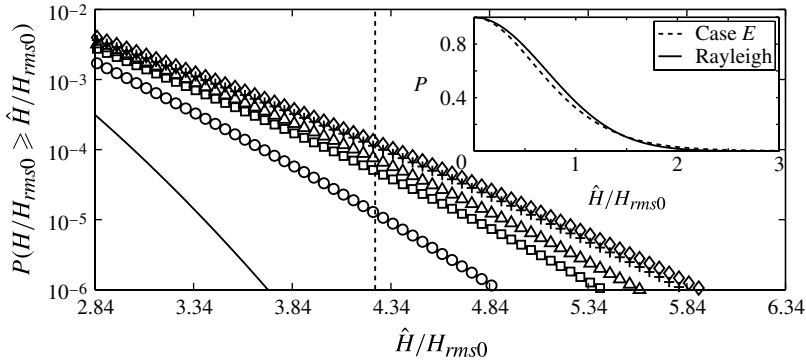
FIGURE 12. Probability of freak waves ($\hat{H}/H_{rms0} \geqslant 2.84$; $\hat{H} \geqslant 2H_s$) for Rayleigh distribution (——) and the probability obtained from the Alber equation (see table 2): case *A*, ($\bigcirc$); case *B*, ($\square$); case *C*, ($\triangle$); case *D*, (+); and case *E*, ($\diamond$). The vertical dashed line represents ($\hat{H}/H_{rms0} \geqslant 4.26$; $\hat{H} \geqslant 3H_s$). The inset shows the probability function for Rayleigh distribution (solid line) and case *E* (dashed line) starting from zero wave height.

from figure 12, case *E* gives 40 of 10 000 waves being higher than $2.84H_{rms0}$ ($\approx 2H_s$), as opposed to case *A* where this is about 17 of 10 000, since this case is closer to the Rayleigh distribution.

Furthermore, as seen from figure 12, the vertical dashed line represents the probability of waves whose heights are higher than three times the significant wave height; the probability values increase from 10^{-8} for the Rayleigh distribution to 10^{-5} for case *A*, 5×10^{-5} for case *B*, 7×10^{-5} for case *C*, 11×10^{-5} for case *D* and 13×10^{-5} for case *E*.

It should be mentioned at this stage that the Alber equation, like the kinetic equation, the Zakharov equation, the nonlinear Schrödinger equation and other equations that deal with nonlinear evolution of water waves, does not have a dissipation mechanism and energy-input mechanism. The kinetic equation, for example, is most broadly employed by wave forecasting models, but is always combined with terms that represent wind energy input and wave-breaking dissipation, among others. Therefore, applying the outcomes of the Alber equation to real waves in the ocean should be done with caution. It is known, both from solutions of the nonlinear Schrödinger equation with energy sources/sinks added and from experiments, that instability of wave trains is altered due to such external forcings (e.g. Trulsen & Dysthe 1992; Galchenko *et al.* 2012; Onorato & Proment 2012). Moreover, in theory, the Alber equation and other equations based on higher-order terms in deep water allow for infinite wave heights to occur. In reality, there is a limit of wave steepness beyond which the waves will break (Babanin *et al.* 2010), and this limit indicates the maximum ratio of individual wave height to the significant wave height of ~ 2.0 (Babanin *et al.* 2011*b*). Note, however, that this maximum ratio was obtained from a one-dimensional quasi-monochromatic wave experiment.

Following a similar procedure to determine the probability of freak waves for the cases with $\gamma = 10$, one obtains figure 13. As seen from figure 13 for the unidirectional JONSWAP spectrum with a peak enhancement $\gamma = 10$ with varying energy scale, case B_4 gives 205 out of 10^5 waves being higher than $2.84H_{rms0}$ ($\approx 2H_s$), as opposed to case B_1, where this is about 95 out of 10^5; the latter case is closer to a Rayleigh distribution with 31 out of 10^5. Similarly, the probability of waves whose heights are
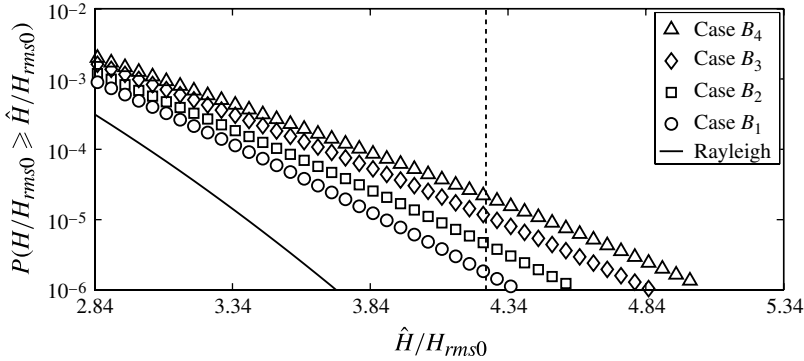
FIGURE 13. Probability of freak waves ($\hat{H}/H_{rms0} \geqslant 2.84$; $\hat{H} \geqslant 2H_s$) for Rayleigh distribution and the probability obtained from the Alber equation (see table 2). The vertical dashed line represents ($\hat{H}/H_{rms0} \geqslant 4.26$; $\hat{H} \geqslant 3H_s$).
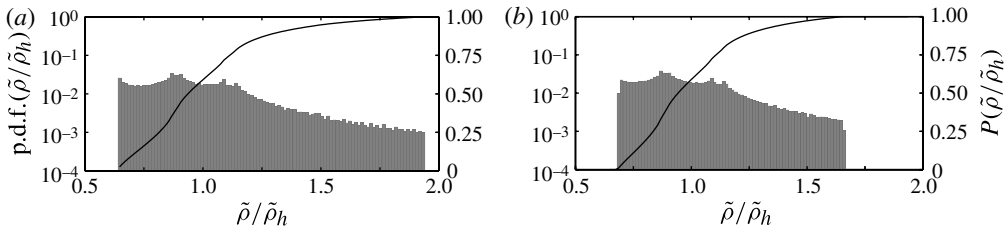

FIGURE 14. Probability density function p.d.f.($\tilde{\rho}/\tilde{\rho}_h$) (histogram) and probability function $P(\tilde{\rho}/\tilde{\rho}_h)$ (solid line) as functions of $\tilde{\rho}/\tilde{\rho}_h$: (*a*) case A_1 and (*b*) case A_2 of table 3.

higher than three times the significant wave height increases from values of 10^{-8} for the Rayleigh distribution to 2×10^{-6} for case B_1, 6×10^{-6} for case B_2, 11×10^{-6} for case B_3 and 21×10^{-6} for case B_4. These cases are indicated by a dashed vertical line.

5.2. *JONSWAP spectrum with a directional distribution*

Following a similar procedure to that used to determine the p.d.f. in the unidirectional case, the p.d.f.s for the JONSWAP spectrum with a directional distribution are shown in figure 14. As one can see, the number of active bins decreases on decreasing the degree of the directional distribution. In other words, the number of active bins reduces when the 'width parameter' Π_2 increases. This trend is consistent with the unidirectional case.

Figure 15 shows the wave-height probability for an inhomogeneous ocean obtained from the Alber equation. These results are for the JONSWAP spectra with the degrees of the directional distribution set at $n = 10$ (case A_2) and $n = 50$ (case A_1) and parameters $\gamma = 10$, $\varepsilon = 0.126$ ($\alpha = 0.016$). Similar to the unidirectional case, one can see from the inset of figure 15 that the probability up to $\hat{H} \geqslant 1.49H_{rms0}$ is greater for the Rayleigh distribution, and after the intersection point the probability is greater for the results obtained from the Alber equation. As one can see, the probability of freak waves with wave height larger than two times the significant wave height is $9/10\,000$ when the degree of the directional distribution is 50 and decreases down to $7/10\,000$
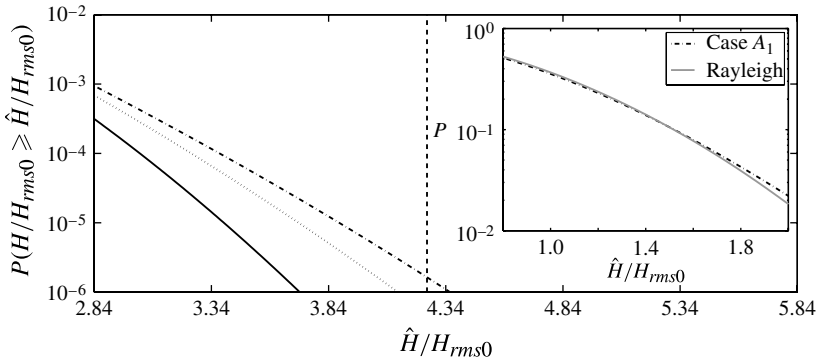
FIGURE 15. Probability of freak waves ($\hat{H}/H_{rms0} \geqslant 2.84$; $\hat{H} \geqslant 2H_s$) for the Rayleigh distribution (——) and the probability obtained from the Alber equation: case A_1, -··-; and case A_2, ····· (see table 3). The vertical dashed line represents ($\hat{H}/H_{rms0} \geqslant 4.26$; $\hat{H} \geqslant 3H_s$).

when the degree of the directional distribution decreases to 10. Overall, this probability is significantly lower than in the unidirectional case.

The reduction is even more significant for the probability of exceptionally high freak waves, with wave heights higher than three times the significant wave height. It is of the order of 10^{-8} for the Rayleigh distribution, 16×10^{-7} for case A_1 and 5×10^{-7} for case A_2, as shown in figure 15, which is indicated by a vertical dashed line. We should note that the maximum wave height limited by wave breaking changes for three-dimensional waves if compared with two-dimensional, because both limiting steepness and limiting skewness of waves are different in three dimensions (Toffoli *et al.* 2010*a*; Babanin *et al.* 2011*a*). Comparing the probability of freak waves with wave heights larger than two times the significant wave height for the unidirectional JONSWAP spectrum as shown in figure 13, with the JONSWAP spectrum with the degree of the directional distribution set at $n = 50$, one can see that the former probability is slightly higher, as expected.

Using these eleven results and four other cases (not shown here), the occurrence probability of freak waves can be estimated by simple relations using the best fit available in MATLAB, that is,

$$P(H_f > 2H_s) = 10^{-(1.80+1.50\Pi)}, \qquad (5.2a)$$

$$P(H_f > 3H_s) = 10^{-(2.00+4.65\Pi)}, \qquad (5.2b)$$

where H_f and H_s are the freak wave height and the significant wave height, respectively. We have $\Pi = \Pi_1 < 1$ and $\Pi = \Pi_2 < 1.1$ for the unidirectional JONSWAP spectrum and JONSWAP spectrum with the directional distribution, respectively. The fact that almost any wave field, with a single peak frequency, can be approximated by a JONSWAP spectrum adds to the applicability of the above-mentioned result. Finally, we have to emphasize that our results for the probability of freak waves are in qualitative agreement with both laboratory results such as Onorato *et al.* (2009*a*) and Waseda *et al.* (2009) and numerical simulations such as Eliasson & Shukla (2010) and Toffoli *et al.* (2010*b*). In particular, all of these previous results from wave flumes and the numerical simulations conclude that the occurrence probability of freak waves decreases when the directional spread of the initial spectrum increases.

6. Summary and conclusions

In this paper, the Alber equation is used to study the evolution of homogeneous wave fields, under the influence of small initial inhomogeneous disturbances. We first conducted an academic test of instability for the two-dimensional symmetric Lorentz spectrum, and then studied instability of realistic ocean-wave asymmetric JONSWAP spectra, both unidirectional and with a directional distribution. The stochastic recurrence, which is parallel to the Fermi–Pasta–Ulam recurrence, and its application to the probability of freak waves were then investigated.

The simple structure of the two-dimensional Lorentz spectrum shows that the maximum growth rate is on $q = 0$, where q is the wavenumber of the disturbance perpendicular to the carrier wave. For such a symmetric spectrum, (2.4) can be solved analytically. However, for asymmetric spectra, such as the JONSWAP spectrum, one has to seek an approximate solution for (2.4). To this end, we have established a 'general method', described in appendix C, and validation of this method is shown in figure 1.

JONSWAP spectra with a directional distribution depend on four basic parameters: k_0, α, γ and n, which are the carrier wavenumber, the energy scale, the peak enhancement and the degree of the directional distribution, respectively. It is instructive to observe that the physical issues of: stability–instability transition, the most unstable mode, recurrence duration and freak-wave probability depend solely on the dimensionless 'width parameter' as defined in (3.8) and (3.12) for unidirectional and for directional wave fields, respectively. It is found that unidirectional JONSWAP spectra and JONSWAP spectra with directional wave energy distributions are stable to inhomogeneous disturbance when the 'width parameters' satisfy $\Pi_1 > 1$ as defined in (3.8) and $\Pi_2 > 1.1$ as defined in (3.12), respectively. Note that, for waves with continuous spectrum, these dimensionless 'widths' offer more possibilities than the traditional Benjamin–Feir index because in the spectral environment the same steepness or the same bandwidth can be achieved by varying different parameters of the spectral shape, which imply different physical meanings.

Furthermore, for instability conditions, we have shown that, for realistic ocean-wave JONSWAP spectra, wave fields exhibit stochastic recurrence analogous to Fermi–Pasta–Ulam recurrence in deterministic quasi-monochromatic cases. Specifically, for the unidirectional JONSWAP spectra, the influence of the energy scales has been investigated, while for JONSWAP spectra with a directional distribution the influence of the degree of the directional spreading has been simulated.

The stochastic recurrence enables us to study the probability of freak waves. It is found that the probability of the freak waves is higher by comparison to the classical values given by the Rayleigh distribution.

It is important to mention that the initial inhomogeneous disturbances that are used in this work were taken to depend on the homogeneous spectra themselves. Namely: (i) the wavenumber of the most unstable mode is a property of the spectrum (see (2.4)); (ii) the function $R(\boldsymbol{r})$ in (2.3) was taken as $\rho_h(\boldsymbol{r})$; and (iii) δ in (2.3) was assigned the value 0.1, which is typically of the order of ε. The influence of different choices of disturbances is demonstrated in Regev *et al.* (2008), Stiassnie *et al.* (2008), and more recently in Eliasson & Shukla (2010).

In order to put our findings into appropriate proportion, it is worthwhile to keep in mind the various choices that we have made in this study. First, we have chosen to explore the Alber equation rather than other possibilities listed in table 1, in order to enrich our knowledge about its possible physical consequences. Second, we have

chosen to study the long-time evolution of unstable homogeneous spectra to their most unstable inhomogeneous disturbance, a choice that resulted in a recurrent solution. Taking either stable homogeneous spectra or other inhomogeneous disturbance is expected to yield a wealth of other types of solutions. To this end, one can refer to the recent work of Stiassnie *et al.* (2008). Third, as mentioned earlier in the section, the specific details of the initial inhomogeneous disturbance were taken to depend on the homogeneous spectra themselves, but other options are possible – see Regev *et al.* (2008). Finally, we took advantage of the periodicity imposed by the initial disturbance and the consequent recurrent evolution of unstable spectra to calculate the probability of freak waves, implying that, for stable spectra, the freak wave probability will be given by the Rayleigh distribution.

To summarize, we are aware that each of the above choices can be open to criticism since alternative choices are available and we thus consider the interesting phenomenon of stochastic recurrence as opening a new avenue in the theory of stochastic weakly nonlinear wave fields, rather than as the generic solution.

Acknowledgements

Appendix A. Numerical approach

It is convenient to change the two spatial dimensions in the Alber equation on infinitely deep water from the dimensional form as in (2.1) to non-dimensional variables using the relations

$$\tilde{\rho} = \frac{k_0^2}{\varepsilon^2}\rho, \quad \tilde{x}_1 = \varepsilon k_0 \left(x_1 - \frac{1}{2}\sqrt{\frac{g}{k_0}}t \right), \quad \tilde{x}_2 = \varepsilon k_0 x_2, \atop \tilde{r}_1 = \varepsilon k_0 r_1, \quad \tilde{r}_2 = \varepsilon k_0 r_2, \quad \tilde{\tau} = \varepsilon^2 \sqrt{gk_0}\, t, \qquad (A\,1)$$

which yields

$$\mathrm{i}\frac{\partial \tilde{\rho}}{\partial \tilde{\tau}} + 2\lambda\frac{\partial^2 \tilde{\rho}}{\partial \tilde{x}_1 \partial \tilde{r}_1} + 2\mu\frac{\partial^2 \tilde{\rho}}{\partial \tilde{x}_2 \partial \tilde{r}_2}$$
$$= 2\nu\tilde{\rho}(\tilde{\boldsymbol{x}}, \tilde{\boldsymbol{r}}, \tilde{\tau})[\tilde{\rho}(\tilde{\boldsymbol{x}} + \tfrac{1}{2}\tilde{\boldsymbol{r}}, \boldsymbol{0}, \tilde{\tau}) - \tilde{\rho}(\tilde{\boldsymbol{x}} - \tfrac{1}{2}\tilde{\boldsymbol{r}}, \boldsymbol{0}, \tilde{\tau})], \qquad (A\,2)$$

where $\lambda = -1/8$, $\mu = 1/4$, $\nu = 1/2$.

For simplicity, only a two-dimensional spectrum and one-dimensional perturbation will be considered. As a result, the third term of (A 2) vanishes automatically and, therefore, the dimensionless Alber equation can be rewritten as

$$\mathrm{i}\frac{\partial \tilde{\rho}}{\partial \tilde{\tau}} + 2\lambda\frac{\partial^2 \tilde{\rho}}{\partial \tilde{x}_1 \partial \tilde{r}_1} - 2\nu\tilde{\rho}(\tilde{x}_1, \tilde{\boldsymbol{r}}, \tilde{\tau})[\tilde{\rho}(\tilde{x}_1 + \tfrac{1}{2}\tilde{r}_1, \boldsymbol{0}, \tilde{\tau}) - \tilde{\rho}(\tilde{x}_1 - \tfrac{1}{2}\tilde{r}_1, \boldsymbol{0}, \tilde{\tau})] = 0,$$
$$(A\,3)$$

where $\tilde{\rho}$ is a function of $\tilde{x}_1$, $\tilde{r}_1$, $\tilde{r}_2$ and $\tilde{\tau}$.

A finite difference method will be used to solve (A 3), where the dimensionless time derivative is approximated by a forward difference and the dimensionless spatial

derivatives in $\tilde{x}_1$ and $\tilde{r}_1$ are approximated by central differences, yielding

$$\text{i}\left(\frac{\tilde{\rho}_{(n,j,k,l+1)} - \tilde{\rho}_{(n,j,k,l)}}{\Delta\tilde{\tau}}\right)$$
$$+ \frac{2\lambda}{4\Delta\tilde{x}_1\Delta\tilde{r}_1}\{\tilde{\rho}_{(n+1,j+1,k,l)} - \tilde{\rho}_{(n-1,j+1,k,l)} - (\tilde{\rho}_{(n+1,j-1,k,l)} - \tilde{\rho}_{(n-1,j-1,k,l)})\}$$
$$- 2\nu\tilde{\rho}_{(n,j,k,l)}(\tilde{\rho}_{(n+j\Delta\tilde{r}_1/2\Delta\tilde{x}_1,0,0,l)} - \tilde{\rho}_{(n-j\Delta\tilde{r}_1/2\Delta\tilde{x}_1,0,0,l)}) = 0. \quad (A\,4)$$

In (A 4) the index n belongs to points along the $\tilde{x}_1$ axis, $\tilde{x}_1 = n\Delta\tilde{x}_1$ ($n = 0, 1, 2, \ldots, N$), and $N + 1$ is the number of points along this axis. The index j represents points along the $\tilde{r}_1$ axis, $\tilde{r}_1 = j\Delta\tilde{r}_1$ ($j = 0, 1, 2, \ldots, M_1$), and $M_1 + 1$ is the number of points along the $\tilde{r}_1$ axis. Similarly, the index k represents points along the $\tilde{r}_2$ axis, $\tilde{r}_2 = k\Delta\tilde{r}_2$ ($k = 0, 1, 2, \ldots, M_2$), and $M_2 + 1$ is the number of points along the $\tilde{r}_2$ axis, and l represents the time steps by $\tilde{\tau} = l\Delta\tilde{\tau}$ ($l = 0, 1, 2, \ldots, T$).

Thus, the numerical time stepping scheme is formulated as follows:

$$\tilde{\rho}_{(n,j,k,l+1)} = \tilde{\rho}_{(n,j,k,l)} + \frac{\text{i}\lambda\Delta\tilde{\tau}}{2\Delta\tilde{x}_1\Delta\tilde{r}_1}\{\tilde{\rho}_{(n+1,j+1,k,l)} - \tilde{\rho}_{(n-1,j+1,k,l)}$$
$$- (\tilde{\rho}_{(n+1,j-1,k,l)} - \tilde{\rho}_{(n-1,j-1,k,l)})\}$$
$$- 2\text{i}\Delta\tilde{\tau}\nu\tilde{\rho}_{(n,j,k,l)}(\tilde{\rho}_{(n+j\Delta\tilde{r}_1/(2\Delta\tilde{x}_1),0,0,l)} - \tilde{\rho}_{(n-j\Delta\tilde{r}_1/(2\Delta\tilde{x}_1),0,0,l)}). \quad (A\,5)$$

The following values for the differential steps were taken after several attempts. For the one-dimensional case, as a special case, the differential steps are: $\Delta\tilde{x}_1 = \pi/100$, $\Delta\tilde{r}_1 = \pi/44$ and $\Delta\tilde{\tau} = 5 \times 10^{-5}$. For the two-dimensional case, the differential steps are: $\Delta\tilde{x}_1 = \pi/75$, $\Delta\tilde{r}_1 = \pi/35$, $\Delta\tilde{r}_2 = \pi/25$ and $\Delta\tilde{\tau} = 4 \times 10^{-5}$. Taking smaller values will not have a significant effect. In addition, the size of the domain for the one-dimensional case is $\tilde{x}_1 \in (0, 2\pi/\tilde{P}_1^{(max)})$, where $\tilde{P}_1^{(max)}$ is the most unstable mode, and after several attempts we choose $\tilde{r}_{1(end)} = 15\tilde{x}_{1(end)}$ and hence $\tilde{r}_1 \in (0, 30\pi/\tilde{P}_1^{(max)})$. For the two-dimensional case, the size of the domain is also $\tilde{x}_1 \in (0, 2\pi/\tilde{P}_2^{(max)})$ and we also choose $\tilde{r}_{1(end)} = 15\tilde{x}_{1(end)}$ and $\tilde{r}_{2(end)} = 15\tilde{x}_{1(end)}$, and hence $\tilde{r}_1 \in (0, 30\pi/\tilde{P}_2^{(max)})$ and $\tilde{r}_2 \in (0, 30\pi/\tilde{P}_2^{(max)})$. In order to decide on the appropriate truncation of the $\tilde{r}_1$ axis, we have taken four different values, namely, $\tilde{r}_{1(end)} = 10\tilde{x}_{1(end)}$, $15\tilde{x}_{1(end)}$, $20\tilde{x}_{1(end)}$ and $30\tilde{x}_{1(end)}$, and compared their influence on the evolution of $\tilde{\rho}_{max}(\tilde{r}_1 = 0)$ and the evolution of the invariants. Based on this small study, we decided to choose $\tilde{r}_{1(end)} = 15\tilde{x}_{1(end)}$ and $\tilde{r}_{2(end)} = 15\tilde{x}_{1(end)}$ in our calculation. We restrict ourselves to periodic solution in $\tilde{x}_1$, so that, on the boundaries $\tilde{x}_1 = \tilde{x}_{1(end)}$, $\tilde{\rho}_{(N,j,k,l)} = \tilde{\rho}_{(0,j,k,l)}$. Moreover, the last term on the right-hand side of (A 5) depends on the values of $\tilde{\rho}$ at $\tilde{x}_1 = n + j\Delta\tilde{r}_1/2\Delta\tilde{x}_1$, which can be larger than $\tilde{x}_{1(end)} = N\Delta\tilde{x}_1$. For this condition, the periodicity, again, is defined such that $\tilde{\rho}(\tilde{x}_1 + 2q\pi, \tilde{r}, \tilde{\tau}) = \tilde{\rho}(\tilde{x}_1, \tilde{r}, \tilde{\tau})$, where $q = 1, 2, 3, \ldots$. This equation can be rewritten as $\tilde{\rho}_{(n+qN,j,k,l)} = \tilde{\rho}_{(n,j,k,l)}$. Similarly, the values of $\tilde{\rho}$ at $\tilde{r} = 0$ depend on points outside the domain $0 \leqslant \tilde{r}_1 \leqslant \tilde{r}_{1(end)}$ and $0 \leqslant \tilde{r}_2 \leqslant \tilde{r}_{2(end)}$. In particular, the terms on the right-hand side of (A 5) depend on $\tilde{\rho}_{(n+1,-1,k,l)}$. In order to deal with these problems, the definition of $\tilde{\rho}$, which is the two-point correlation function in (1.3), will be used, that is, $\tilde{\rho}(\tilde{x}_1, \tilde{r}, \tilde{\tau}) = \tilde{\rho}^*(\tilde{x}_1, -\tilde{r}, \tilde{\tau})$. Therefore, the values of $\tilde{\rho}$ along $\tilde{r} = 0$ can be calculated from the conditions $\tilde{\rho}_{(n+1,-1,k,l)} = \tilde{\rho}^*_{(n+1,1,k,l)}$. Moreover, theoretically, the values of spacing, $\tilde{r}$, are from negative infinity to infinity, or all real numbers. However, using the symmetrical

properties, the values of $\tilde{r}$ can be taken from zero to infinity. For numerical purposes, $\tilde{r}$ has to be truncated. Following a similar approach to equation (3.2) of Stiassnie *et al.* (2008), one will end up with the following equation:

$$\rho(x_1, \boldsymbol{r}, \tau) = \int_{-\infty}^{\infty} \mathrm{e}^{\mathrm{i}(k-k_0)\cdot\boldsymbol{r}} \sqrt{S(\boldsymbol{k}, x_1 + r_1/2, \tau)\, S(\boldsymbol{k}, x_1 - r_1/2, \tau)} \, \mathrm{d}\boldsymbol{k}. \quad (A\,6)$$

We now approximate $S(\boldsymbol{k}, x_1)$ by a two-dimensional rectangular spectrum in $(k_1 - k_0) \in (-W_l, W_r)$ and $k_2 \in (-W, W)$, where W_l and W_r are the spectral widths on the left-hand and right-hand sides of k_0, which is the carrier, while W is the spectral width, which is perpendicular to the carrier. Integrating and switching to dimensionless quantities leads to the boundary condition used at large $\tilde{r}_1$ or $\tilde{r}_2$:

$$\tilde{\rho}(\tilde{x}_1, \tilde{\boldsymbol{r}}, \tilde{\tau}) = \sqrt{\rho(\tilde{x}_1 + \tilde{r}_1/2, \boldsymbol{0}, \tilde{\tau})\, \tilde{\rho}(\tilde{x}_1 - \tilde{r}_1/2, \boldsymbol{0}, \tilde{\tau})} \left(\frac{\sin(\tilde{W}\tilde{r}_2)}{\tilde{W}\tilde{r}_2}\right) \left(\frac{\mathrm{e}^{\mathrm{i}\tilde{W}_r\tilde{r}_1} - \mathrm{e}^{-\mathrm{i}\tilde{W}_l\tilde{r}_1}}{\mathrm{i}(\tilde{W}_l + \tilde{W}_r)\tilde{r}_1}\right). \quad (A\,7)$$

In order to determine the values of $\tilde{W}$, $\tilde{W}_l$ and $\tilde{W}_r$, one needs to compare the rectangular spectrum with the JONSWAP spectrum by maintaining that both spectra must have the same total energy and momentum.

As one can see from (A 5), this problem is defined for a four-dimensional space. Therefore, it requires huge computer memory and a long computational time. Thus, a parallel programming solution is necessary. To this end, we use OpenMP (Open Multi-Processing), which allows us to spread the jobs over the processors in one node. For the one-dimensional problem, which only contains a three-dimensional space, we use eight processors and it takes a few hours to complete the job. However, for the two-dimensional case, we use 16 processors and it takes more than two weeks to complete one job.

Appendix B. Derivation of the invariants

The invariants in (2.5)–(2.7) were derived as follows.

First invariant

Evaluating (2.1) at $\boldsymbol{r} = \boldsymbol{0}$ gives

$$\mathrm{i}\left(\frac{\partial\rho}{\partial t} + \frac{1}{2}\sqrt{\frac{g}{k_0}}\frac{\partial\rho}{\partial x_1}\right) - \frac{1}{4}\sqrt{\frac{g}{k_0^3}}\left(\frac{\partial^2\rho}{\partial x_1\partial r_1} - 2\frac{\partial^2\rho}{\partial x_2\partial r_2}\right) = 0. \quad (B\,1)$$

Integrating (B 1) over the two-dimensional domain $x_1 \in [0, 2\pi/p]$, $x_2 \in [0, 2\pi/q]$ and applying the periodicity yields

$$I_1 = \int \rho(\boldsymbol{x}, \boldsymbol{r}, t)\Big|_{\boldsymbol{r}=\boldsymbol{0}} \, \mathrm{d}\boldsymbol{x}, \quad (B\,2)$$

which is related to the wave action.

For all cases in this paper, the first invariant, I_1, did not change at all times from its value at $t = 0$ throughout the calculations.

Second invariant

The second invariant consists of two components. The first component of this invariant is defined by taking the first-order partial derivative of (2.1) with respect

to r_1, that is, $\partial/\partial r_1$, and evaluating at $\boldsymbol{r} = \boldsymbol{0}$, which gives

$$\mathrm{i}\left(\frac{\partial^2 \rho}{\partial r_1 \partial t} + \frac{1}{2}\sqrt{\frac{g}{k_0}}\frac{\partial^2 \rho}{\partial r_1 \partial x_1}\right) - \frac{1}{4}\sqrt{\frac{g}{k_0^3}}\left(\frac{\partial^3 \rho}{\partial x_1 \partial r_1^2} - 2\frac{\partial^3 \rho}{\partial r_1 \partial x_2 \partial r_2}\right)$$
$$= \frac{\sqrt{gk_0^5}}{2}\frac{\partial}{\partial x}(\rho^2(\boldsymbol{x}, \boldsymbol{0}, t)). \tag{B 3}$$

Again, integrating (B 3) over the two-dimensional domain $x_1 \in [0, 2\pi/p]$, $x_2 \in [0, 2\pi/q]$ and applying the periodicity yields

$$I_{21} = \int \frac{\partial \rho(\boldsymbol{x}, \boldsymbol{r}, t)}{\partial r_1}\bigg|_{\boldsymbol{r}=\boldsymbol{0}} \, \mathrm{d}\boldsymbol{x}, \tag{B 4}$$

which is related to the wave momentum along r_1.

Similarly, taking the first-order partial derivative of (2.1) with respect to r_2, that is, $\partial/\partial r_2$, evaluating at $\boldsymbol{r} = \boldsymbol{0}$ and then integrating over the two-dimensional domain $x_1 \in [0, 2\pi/p]$, $x_2 \in [0, 2\pi/q]$ gives

$$I_{22} = \int \frac{\partial \rho(\boldsymbol{x}, \boldsymbol{r}, t)}{\partial r_2}\bigg|_{\boldsymbol{r}=\boldsymbol{0}} \, \mathrm{d}\boldsymbol{x}, \tag{B 5}$$

which is related to the wave momentum along r_2.

For the first part of the second invariant, one can easily show that its value at $t = 0$ is imaginary. The relative deviation of the imaginary part of I_{21} at all times from its value at $t = 0$ did not exceed 1.0% for the one-dimensional case throughout all calculated evolutions and did not exceed 1.5% for the two-dimensional case.

Moreover, for the second part of the second invariant, which appears for the two-dimensional cases, $I_{22} = 0$ since $\rho(t = 0)$ is real and symmetric in r_2. Thus, one cannot compare the values of I_{22} at all times to the initial value.

Third invariant

To obtain the explicit formula for this invariant, first, taking the second-order partial derivative of (2.1) with respect to r_1, that is, $\partial^2/\partial r_1^2$, evaluating at $\boldsymbol{r} = \boldsymbol{0}$ and integrating over the two-dimensional domain $x_1 \in [0, 2\pi/p]$, $x_2 \in [0, 2\pi/q]$ as well as applying the periodicity yields

$$\mathrm{i}\frac{\partial \rho}{\partial t}\left(\int \frac{\partial^2 \rho}{\partial r_1^2} \, \mathrm{d}\boldsymbol{x}\right) = 2\sqrt{gk_0^5}\int \frac{\partial \rho}{\partial r_1}\frac{\partial \rho}{\partial x_1} \, \mathrm{d}\boldsymbol{x}. \tag{B 6}$$

Applying a similar procedure to r_2 gives

$$\mathrm{i}\frac{\partial \rho}{\partial t}\left(\int \frac{\partial^2 \rho}{\partial r_2^2} \, \mathrm{d}\boldsymbol{x}\right) = 2\sqrt{gk_0^5}\int \frac{\partial \rho}{\partial r_2}\frac{\partial \rho}{\partial x_2} \, \mathrm{d}\boldsymbol{x}. \tag{B 7}$$

Evaluating (2.1) at $\boldsymbol{r} = \boldsymbol{0}$, then multiplying by ρ and integrating over $\boldsymbol{x}$ yields

$$\mathrm{i}\int\left(\rho\frac{\partial \rho}{\partial t} + \frac{1}{2}\sqrt{\frac{g}{k_0}}\rho\frac{\partial \rho}{\partial x_1}\right) \, \mathrm{d}\boldsymbol{x} = \frac{1}{4}\sqrt{\frac{g}{k_0^3}}\int\left(\rho\frac{\partial^2 \rho}{\partial x_1 \partial r_1} - 2\rho\frac{\partial^2 \rho}{\partial x_2 \partial r_2}\right) \, \mathrm{d}\boldsymbol{x}. \tag{B 8}$$

Integrating the right-hand side of this equation by parts over $\boldsymbol{x}$, and applying the periodicity yields

$$\frac{\mathrm{i}}{2}\int \frac{\partial \rho^2}{\partial t} \, \mathrm{d}\boldsymbol{x} + \frac{1}{4}\sqrt{\frac{g}{k_0^3}}\int\left(\frac{\partial \rho}{\partial r_1}\frac{\partial \rho}{\partial x_1}\right) \, \mathrm{d}\boldsymbol{x} - \frac{1}{2}\sqrt{\frac{g}{k_0^3}}\int\left(\frac{\partial \rho}{\partial r_2}\frac{\partial \rho}{\partial x_2}\right) \, \mathrm{d}\boldsymbol{x} = 0. \tag{B 9}$$

Substituting (B 6) and (B 7) into (B 9) gives the third invariant as

$$I_3 = \int \rho^2(\boldsymbol{x}, \boldsymbol{r}, t)\bigg|_{r=0} \, \mathrm{d}\boldsymbol{x} + \frac{1}{4k_0^4} \int \frac{\partial^2 \rho(\boldsymbol{x}, \boldsymbol{r}, t)}{\partial r_1^2}\bigg|_{r=0} \, \mathrm{d}\boldsymbol{x}$$
$$- \frac{1}{2k_0^4} \int \frac{\partial^2 \rho(\boldsymbol{x}, \boldsymbol{r}, t)}{\partial r_2^2}\bigg|_{r=0} \, \mathrm{d}\boldsymbol{x}, \tag{B 10}$$

which is related to the energy of the system.

The relative deviation of I_3 at all times from its value at $t = 0$ did not exceed 1.0 % for the one-dimensional case throughout all calculated evolutions, and did not exceed 1.1 % for the two-dimensional cases.

Appendix C. Approximate solution of (2.4) for general spectra

In order to determine the maximum growth rate and the point of maximum growth of any spectrum, it is substituted into (2.4). However, since this integral cannot be solved analytically for an asymmetric spectrum such as a JONSWAP spectrum, it is necessary to seek an approximate solution. To this end, the original spectrum $s(k)$ will be replaced by a sum of weighted Dirac delta functions as follows:

$$s(k) = \sum_{l_{min}}^{l_{max}} s_l \delta(k - k_l), \tag{C 1}$$

where $k_l = l\Delta k$, $s_l = s(k_l)\Delta k$ and $l = 1, 2, 3, \ldots, L$.

Substituting this equation into (2.4) for a one-dimensional case, i.e. $q = 0$, gives

$$l = 4k_0^4 p^2 \sum_{l_{min}}^{l_{max}} \frac{s_l}{\dfrac{p^4}{4} - \left[p(k_l - k_0) + \dfrac{4k_0^2\Omega}{\sqrt{gk_0}}\right]^2}. \tag{C 2}$$

Note that all of the quantities in (C 2) have numerical values, and that only Ω is unknown. Moreover, using MATLAB, this equation can be reduced to a polynomial equation of order $L = 2(l_{max} - l_{min} + 1)$, that is,

$$\sum_{\mu=0}^{L} a_\mu \Omega^\mu = 0, \tag{C 3}$$

where a_μ are the constant coefficients of the polynomial. However, the highest-order algebraic equation that can be used is $L = 70$, owing to the limitation of MATLAB to solve the polynomial for these cases. Note that the convergence has been checked by taking $L = 30, 40, 50, 60$ and 70. Furthermore, seeking the root for Ω with the largest imaginary contribution will give the maximum growth rate of the given spectrum. From this, one can also get the point of maximum growth. The validity of this rather 'general method' is demonstrated by using the one-dimensional counterpart of the Lorentz spectrum as given in (3.1) with the growth rate as given in (3.5b).

In order to apply the 'general method' to the Lorentz spectrum, the following procedure was carried out. As known, the limit of k is along the real numbers, but, for numerical reasons, it has to be truncated. Therefore, let k_{min} and k_{max} be the lower limit and the upper limit of k, respectively; then Δk is defined as

$$\Delta k = \frac{k_{max} - k_{min}}{L} \tag{C 4}$$

and thus

$$s_l = s(k_l)(\Delta k) = \left(\frac{W_1 a_0^2}{2\pi[(k_l - k_0)^2 + W_1^2]} \right) \left(\frac{k_{max} - k_{min}}{L} \right), \tag{C 5}$$

where

$$k_l = k_{min} + \left(\frac{k_{max} - k_{min}}{L} \right) \left(l - \frac{1}{2} \right), \quad l = 1, 2, 3, \dots, L. \tag{C 6}$$

The validation of this 'general method' is shown in figure 1.

Appendix D. Dimensional considerations leading to the definition of the width parameter

In order to obtain the dimensionless width parameter, a dimensional analysis approach is performed in the following. Let $\Omega_1^{(max)}$ be the growth rate of the most unstable disturbance, which depends on the physical quantities, namely, the acceleration due to the gravity, g, the total energy, $a_0^2/2$, the peak wavenumber, k_0, and the spectral width, W, which is defined as the quotient of the total energy to the spectral peak s_0. In particular, for a unidirectional JONSWAP spectrum, $s_0 = \alpha\gamma e^{-1.25}/(2k_0^3)$ and $W = a_0^2 k_0^3/(\alpha\gamma e^{-1.25})$. Thus, there must exist a function

$$f(\Omega_1^{(max)}, g, a_0^2/2, k_0, a_0^2 k_0^3/(\alpha\gamma e^{-1.25})) = 0. \tag{D 1}$$

Using k_0 and g as fundamental quantities, Buckingham's Pi theorem (Buckingham 1914) assures the existence of the function

$$f_1(\Omega_1^{(max)}/\sqrt{gk_0}, \varepsilon^2, \varepsilon^2/\alpha\gamma) = 0, \tag{D 2}$$

where $\varepsilon = a_0 k_0 = o(1)$ is a typical wave steepness. Without loss of generality, f_1 can be replaced by

$$f_2 \left(\frac{\Omega_1^{(max)}}{\varepsilon^2 \sqrt{gk_0}}, \frac{\varepsilon}{\alpha\gamma}, \varepsilon \right) = 0. \tag{D 3}$$

In this equation, $\Omega_1^{(max)}/\varepsilon^2\sqrt{gk_0}$ and $\varepsilon/\alpha\gamma$ are both usually of $O(1)$ whereas ε is $o(1)$, so that approximately

$$\frac{\Omega_1^{(max)}}{\varepsilon^2 \sqrt{gk_0}} = f_3 \left(\frac{\varepsilon}{\alpha\gamma} \right). \tag{D 4}$$

As seen from (D 4), $\Omega_1^{(max)}/\varepsilon^2\sqrt{gk_0}$, which is the dimensionless maximum growth rate, is a function of $\varepsilon/\alpha\gamma$, which we call the dimensionless width parameter, $\Pi_1 = \varepsilon/\alpha\gamma$ for a unidirectional JONSWAP spectrum.

By approximating the JONSWAP spectrum by a Lorentz spectrum (see Onorato *et al.* 2003 for review), one can prove that $\varepsilon/\alpha\gamma = 1$, which corresponds to the case of marginal stability. For infinitely deep water, the most unstable mode occurs at $q = 0$, where q is the wavenumber of the disturbance perpendicular to the carrier wave. This enables us to replace the study of two-dimensional spectra, $S(k_1, k_2)$, by reducing the problem to its one-dimensional equivalent, $s(k_1)$, using the following relation:

$$s(k_1) = \int_{-\infty}^{\infty} S(k_1, k_2) \, dk_2. \tag{D 5}$$

Therefore, for two-dimensional JONSWAP spectra, the dimensionless parameter $\Pi_1 = \varepsilon/\alpha\gamma$ needs only a slight correction to

$$\Pi_2 = \frac{\varepsilon}{\alpha\gamma} + \frac{0.0256}{\varepsilon A_d}, \quad A_d = \frac{\Gamma(1 + n/2)}{\sqrt{\pi}\,\Gamma(1/2 + n/2)}. \tag{D 6}$$

Note that $\varepsilon/\alpha\gamma$ and $1/\varepsilon A_d$ are the dimensionless scaled widths in the peak direction and the transverse direction, respectively. The transverse scaled width $1/\varepsilon A_d$ arises naturally when the energy $a_0^2/2$ is divided by the spectral peak $s_0 = \alpha\gamma A_d \mathrm{e}^{-1.25}/(2k_0^3)$ as well as by the spectral width $W = a_0^2 k_0^3/(\alpha\gamma \mathrm{e}^{-1.25})$ and finally scaled by ε.

REFERENCES

ALBER, I. E. 1978 The effects of randomness on the stability of two-dimensional surface wavetrains. *Proc. R. Soc. Lond.* A **363**, 525–546.

BABANIN, A. 2011 *Breaking and Dissipation of Ocean Surface Waves*, p. 485. Cambridge University Press.

BABANIN, A. V., CHALIKOV, D., YOUNG, I. R. & SAVELYEV, I. 2010 Numerical and laboratory investigation of breaking of steep two-dimensional waves in deep water. *J. Fluid Mech.* **644**, 433–463.

BABANIN, A. V. & SOLOVIEV, Y. P. 1987 Parameterization of the width of angular-distribution of the wind wave energy at limited fetches. *Izv. Akad. Nauk SSSR Fiz. Atmos. Okeana* **23**, 868–876.

BABANIN, A. V. & SOLOVIEV, Y. P. 1998*a* Field investigation of transformation of the wind wave frequency spectrum with fetch and the stage of development. *J. Phys. Oceanogr.* **28**, 563–576.

BABANIN, A. V. & SOLOVIEV, Y. P. 1998*b* Variability of directional spectra of wind-generated waves, studied by means of wave staff arrays. *Mar. Freshwat. Res.* **49**, 89–101.

BABANIN, A. V., WASEDA, T., KINOSHITA, T. & TOFFOLI, A. 2011*a* Wave breaking in directional fields. *J. Phys. Oceanogr.* **41**, 145–156.

BABANIN, A. V., WASEDA, T., SHUGAN, I. & HWUNG, H.-H. 2011*b* Modulational instability in directional wave fields and extreme wave events. In *Proceedings of the ASME 2011 30th International Conference on Ocean, Offshore and Arctic Engineering, OMAE2011, 19–24 July 2011 Rotterdam, The Netherlands*, *Paper no.* OMAE2011-49540, pp. 409–415. American Society of Mechanical Engineers.

BUCKINGHAM, E. 1914 On physically similar systems; illustrations of the use of dimensional equations. *Phys. Rev.* **4**, 345–376.

CRAWFORD, D. R., SAFFMAN, P. G. & YUEN, H. C. 1980 Evolution of a random inhomogeneous field of nonlinear deep-water gravity waves. *Wave Motion* **2**, 1–16.

DYSTHE, K. B., TRULSEN, K., KROGSTAD, H. E. & SOCQUET-JUGLARD, H. 2003 Evolution of a narrow-band spectrum of random surface gravity waves. *J. Fluid Mech.* **478**, 1–10.

ELIASSON, B. & SHUKLA, P. K. 2010 Numerical investigation of the instability and nonlinear evolution of narrow-band directional ocean waves. *Phys. Rev. Lett.* **105**, 014501.

GALCHENKO, A., BABANIN, A. V., CHALIKOV, D., YOUNG, I. R. & HAUS, B. K. 2012 Influence of wind forcing on modulation and breaking of one-dimensional deep-water wave groups. *J. Phys. Oceanogr.* **42**, 928–939.

GRAMSTAD, O. & TRULSEN, K. 2007 Influence of crest and group length on the occurrence of freak waves. *J. Fluid Mech.* **582**, 463–472.

HASSELMANN, K. 1962 On the non-linear energy transfer in a gravity-wave spectrum, Part 1. General theory. *J. Fluid Mech.* **12**, 481–500.

HOLTHUIJSEN, L. H. 2007 *Waves in Oceanic and Coastal Waters*. Cambridge University Press.

JANSSEN, P. A. E. M. 1981 Modulational instability and the Fermi–Pasta–Ulam recurrence. *Phys. Fluids* **24**, 23–26.

JANSSEN, P. A. E. M. 2003 Nonlinear four-wave interactions and freak waves. *J. Phys. Oceanogr.* **33**, 863–884.

KHARIF, C. & PELINOVSKY, E. 2003 Physical mechanisms of the rogue wave phenomenon. *Eur. J. Mech.* B/*Fluids* **22**, 603–634.

KOMEN, G. J., CAVALERI, L., DONELAN, M., HASSELMANN, K., HASSELMANN, S. & JANSSEN, P. A. E. M. 1994 *Dynamics and Modelling of Ocean Waves*. Cambridge University Press.

LANDSBERG, H. E. 1955 *Advances in Geophysics*, vol. 2. Elsevier.

LONGUET-HIGGINS, M. S. 1952 On the statistical distribution of the heights of sea waves. *J. Mar. Res.* **11**, 245–266.

LONGUET-HIGGINS, M. S. 1976 On the nonlinear transfer of energy in the peak of a gravity-wave spectrum: a simplified model. *Proc. R. Soc. Lond.* A **347**, 311–328.

MORI, N., ONORATO, M. & JANSSEN, P. A. E. M. 2011 On the estimation of the kurtosis in directional sea states for freak wave forecasting. *J. Phys. Oceanogr.* **41**, 1484–1497.

MORI, N., ONORATO, M., JANSSEN, P. A. E. M., OSBORNE, A. R. & SERIO, M. 2007 On the extreme statistics of long-crested deep water waves: theory and experiments. *J. Geophys. Res.* **112**, C09011 doi:10.1029/2006JC004024.

ONORATO, M., CAVALERI, L., FOUQUES, S., GRAMSTAD, O., JANSSEN, P. A. E. M., MONBALIU, J., OSBORNE, A. R., PAKOZDI, C., SERIO, M., STANSBERG, C. T., TOFFOLI, A. & TRULSEN, K. 2009*a* Statistical properties of mechanically generated surface gravity waves: a laboratory experiment in a three-dimensional wave basin. *J. Fluid Mech.* **627**, 235–257.

ONORATO, M., OSBORNE, A., FEDELE, R. & SERIO, M. 2003 Landau damping and coherent structures in narrow-banded $1 + 1$ deep water gravity waves. *Phys. Rev.* E **67**, 046305.

ONORATO, M., OSBORNE, A. R. & SERIO, M. 2002 Extreme wave events in directional, random oceanic sea states. *Phys. Fluids* **14**, 25–28.

ONORATO, M., OSBORNE, A. R., SERIO, M. & BERTONE, S. 2001 Freak waves in random oceanic sea states. *Phys. Rev. Lett.* **86**, 5831–5834.

ONORATO, M., OSBORNE, A. R., SERIO, M., CAVALERI, L., BRANDINI, C. & STANSBERG, C. T. 2004 Observation of strongly non-Gaussian statistics for random sea surface gravity waves in wave flume experiments. *Phys. Rev.* E **70**, 067302.

ONORATO, M. & PROMENT, D. 2012 Approximate rogue wave solutions of the forced and damped nonlinear Schrödinger equation for water waves. *Phys. Lett.* A **376**, 3057–3059.

ONORATO, M., WASEDA, T., TOFFOLI, A., CAVALERI, L., GRAMSTAD, O., JANSSEN, P. A. E. M., KINOSHITA, T., MONBALIU, J., MORI, N., OSBORNE, A. R., SERIO, M., STANSBERG, C. T., TAMURA, H. & TRULSEN, K. 2009*b* Statistical properties of directional ocean waves: the role of the modulational instability in the formation of extreme events. *Phys. Rev. Lett.* **102**, 114502.

PIERSON, W. J. 1955 Wind generated gravity waves. *Adv. Geophys.* **2**, 93–178.

REGEV, A., AGNON, Y., STIASSNIE, M. & GRAMSTAD, O. 2008 Sea-swell interaction as a mechanism for the generation of freak waves. *Phys. Fluids* **20**, 112102.

SOCQUET-JUGLARD, H., DYSTHE, K., TRULSEN, K., KROGSTAD, H. E. & LIU, J. 2005 Probability distributions of surface gravity waves during spectral changes. *J. Fluid Mech.* **542**, 195–216.

STIASSNIE, M. & KROSZYNSKI, U. I. 1982 Long-time evolution of an unstable water-wave train. *J. Fluid Mech.* **116**, 207–225.

STIASSNIE, M., REGEV, A. & AGNON, Y. 2008 Recurrent solutions of Alber's equation for random water-wave fields. *J. Fluid Mech.* **598**, 245–266.

TOFFOLI, A., BABANIN, A., ONORATO, M. & WASEDA, T. 2010*a* Maximum steepness of oceanic waves: field and laboratory. *Geophys. Res. Lett.* **37**, L05603 doi:10.1029/2009GL041771.

TOFFOLI, A., GRAMSTAD, O., TRULSEN, K., MONBALIU, J., BITNER-GREGERSEN, E. & ONORATO, M. 2010*b* Evolution of weakly nonlinear random directional waves: laboratory experiments and numerical simulations. *J. Fluid Mech.* **664**, 313–336.

TRULSEN, K. & DYSTHE, K. 1992 Action of windstress and breaking on the evolution of a wavetrain. In *Breaking Waves* (ed. M. Banner & R. Grimshaw), pp. 243–249. Springer.

WASEDA, T., KINOSHITA, T. & TAMURA, H. 2009 Evolution of a random directional wave and freak wave occurrence. *J. Phys. Oceanogr.* **39**, 621–639.

YOUNG, I. R. 1999 *Wind Generated Ocean Waves*. Elsevier Science.

YUEN, H. C. & FERGUSON, W. E. Jr. 1978*a* Fermi–Pasta–Ulam recurrence in the two-space dimensional nonlinear Schrödinger equation. *Phys. Fluids* **21**, 2116–2118.

YUEN, H. C. & FERGUSON, W. E. Jr. 1978*b* Relationship between Benjamin–Feir instability and recurrence in the nonlinear Schrödinger equation. *Phys. Fluids* **21**, 1275–1278.

ZAKHAROV, V. E. 1968 Stability of periodic waves of finite amplitude on the surface of a deep fluid. *J. Appl. Mech. Tech. Phys.* **9**, 190–194.